Testing General Relativity Using Millimeter Wavelength Radio Interferometry of Sgr A*

by

Jessica Dawn Ruprecht

Submitted to the Department of Earth, Atmospheric, and Planetary Sciences
in partial fulfillment of the requirements for the degree of

Bachelor of Science in Earth, Atmospheric, and Planetary Sciences

at the

MASSACHUSETTS INSTITUTE OF TECHNOLOGY

June 2012

Author ... Signature redacted .....
Department of Earth, Atmospheric, and Planetary Sciences
May 21, 2012

Certified by. Signature redacted .....
Richard P. Binzel
Professor of Planetary Sciences
Thesis Supervisor

Signature redacted

Accepted by ... .
Samuel Bowring
Chair, Committee on Undergraduate Program

Testing General Relativity Using Millimeter Wavelength Radio Interferometry of Sgr A*

by

Jessica Dawn Ruprecht

Submitted to the Department of Earth, Atmospheric, and Planetary Sciences
on May 21, 2012, in partial fulfillment of the
requirements for the degree of
Bachelor of Science in Earth, Atmospheric, and Planetary Sciences

Abstract

General relativity, though widely accepted in the weak-field limit, is difficult to test in the strong-field regime. Millimeter wavelength VLBI offers a unique opportunity to resolve the black hole structure on event-horizon scales. The ability of millimeter wavelength VLBI observations of Sgr A* to constrain black hole parameters such as mass, spin, and deviation from general relativity was considered. Realistic simulations of Sgr A* were performed using the MAPS software. Image reconstructions were made using MACIM and image-based parameter extraction using the Hough transform was considered. Non-imaging techniques using least-squares fitting of a simple ring and gaussian model to VLBI amplitudes and closure phases were considered. The Hough transform is not able to place strong constraints on black hole parameters. Least-squares fitting techniques indicate possible sensitivity to deviations from general relativity and prove able to extract the photon ring radius to within 5-7% of the expected value. It is concluded that VLBI observations of Sgr A* represent a promising opportunity for testing general relativity in the strong-field regime.

Thesis Supervisor: Richard P. Binzel
Title: Professor of Planetary Sciences

Acknowledgments

I would like to thank Shep Doeleman and Vincent Fish for their guidance and support throughout this project. I would also like to thank Scott Hughes for lending his expertise in the field of general relativity. And last but not least, I would like to acknowledge Simone Agha, Editor Extraordinaire, for her invaluable contributions to the coherence of this work. Without their efforts this thesis could not have been completed.

Contents

1 Introduction **13**

1.1 A history of testing general relativity 14

1.1.1 Weak-field confirmation of general relativity 14

1.1.2 Strong-field tests of general relativity 15

1.2 Testing general relativity using the Event Horizon Telescope 16

1.2.1 Defining the photon orbit and the black hole shadow 16

1.2.2 The no-hair theorem, the Kerr metric, and perturbations of general relativity 17

1.2.3 Shadow shape as a function of perturbations on general relativity 18

1.2.4 Photon ring radius as a function of black hole mass and spin . 19

1.2.5 Technological advances necessary to test general relativity . . 20

2 Methods **23**

2.1 Observing astrophysical sources using VLBI 23

2.2 Interstellar scattering and its effect on observation of Sgr A* 26

2.3 Simulating VLBI observations using MAPS software 27

2.4 Image reconstruction using MACIM 30

2.5 Fitting for photon ring size using a Hough transform 31

2.5.1 Understanding the Hough transform 32

2.5.2 Finding circles using the Hough transform 34

2.6 Least-squares fitting of models in the (u, v)-plane 36

2.6.1 Fitting of a ring+gaussian model to simulated datasets 36

3 Results **39**

3.1 Re-imaged models from MACIM 39

3.2 Fitted circles using Hough transform 40

3.3 Ring+Gaussian least-squares fitting results 42

4 Analysis **45**

4.1 Analysis of Hough transform data 45

4.1.1 Determining sensitivity of Hough transform methods to changes in ϵ 45

4.1.2 Determining spin sensitivity 46

4.1.3 Black hole mass determination from Hough transform methods 47

4.2 Analysis of ring+gaussian fitting results 49

4.2.1 Testing for goodness of fit 49

4.2.2 Understanding the χ^2 trends 49

4.2.3 Determining black hole mass from ring+gaussian fitting 52

4.2.4 Determining sensitivity to photon ring size as a function of black hole spin 52

5 Discussion **55**

5.1 Summary of important results 55

5.2 Possibilities for future work 57

5.3 Conclusions 57

A Original and MACIM output images **59**

B Raw data from finding circles using the Hough transform **67**

C Binned Hough transform data **75**

List of Figures

1-1 **Photon ring shape as a function of deviation from general relativity.** 19

2-1 **A simple two element interferometer.** 24

2-2 **(u, v)-coverage of the EHT array used in this thesis.** 26

2-3 **A sample image from Broderick's models.** 28

2-4 **Telescope positions of EHT array.** 29

2-5 **Comparing original input models with re-imaged MACIM results.** 31

2-6 **Illustrating the Hough transform.** 33

2-7 **An example best circle found using the Hough transform.** . . 35

2-8 **Illustrating the ring+gaussian model.** 37

3-1 **Comparing MACIM MODE results with original models.** . . 40

3-2 **Mean Hough transform radius for binned ϵ regimes.** 41

3-3 **Mean Hough transform radius for binned spin regimes.** . . . 42

3-4 **Results from ring+gaussian least-squares fitting methods.** . . 43

3-5 **Results from fitting using ring+gaussian model for all spins.** 43

3-6 **Fitted radius as a function of both ϵ and spin using least-squares methods.** 44

4-1 **An example of the Hough transform finding the outer edge of the accretion disk.** 48

4-2 **Comparing flux density vs. baseline for the best ring+gaussian model and the the simulated VLBI data.** 50

A-1 **Theoretical models vs. MACIM results for all inclinations and ϵ.** 62

A-2 **Theoretical models vs. MACIM results for all inclinations and spins.** 65

List of Tables

2.1 **Input values for each of the eight telescopes included in the EHT array used in this project.** 29

2.2 **The observation specifications input into MAPS simulations.** 29

2.3 **Parameters used on all model image reconstructions in MACIM.** 31

4.1 **Results of computing the mean and standard deviation of detected circle radii across all ϵ at a given inclination.** 47

B.1 **Data from finding circles in MACIM images using the Hough transform.** 67

C.1 **Results of binning data into regimes of small, large positive, and large negative ϵ.** 76

C.2 **Binned radius data for high and low spin regimes at different inclinations.** 76

Chapter 1

Introduction

The theory of general relativity is one of the best-tested and most widely accepted theories in modern physics. However, due to experimental practicalities, the majority of the experiments testing relativity have been performed in the weak-field limit and not in regions with strong gravitational fields. Only recently have observational experiments in astrophysics begun to probe the strong-field regime and thus provide a test of general relativity in extreme cases. One such method for testing general relativity lies in the use of very long baseline interferometry (VLBI) at millimeter and submillimeter radio wavelengths to image black holes on event horizon scales. VLBI uses a global network of radio dishes which can be combined to form an Earth-sized interferometric imaging array. To better constrain the utility of this technique in answering questions of physical behavior in regions with extreme gravitational fields, it is necessary to explore the abilities and limitations of such observations through the use of realistic simulations. The work presented in this thesis will attempt to place bounds on how realistic observations of Sgr A* using sub-millimeter radio astronomy and subsequent image reconstruction can be used to determine black hole parameters such as mass and spin. Additionally, this work attempts to constrain the utility of testing for evidence of deviation from a spacetime described by Einstein's theory of general relativity using these techniques.

1.1 A history of testing general relativity

Experimental tests of general relativity have been performed since Einstein's publication of his theory in 1916. However, it was not until the 1960s that technological advances based on quantum mechanics, such as semiconductors and lasers, as well as the development of the computer, made possible the kind of sensitive experiments necessary to thoroughly and precisely verify the theory's correctness [28].

1.1.1 Weak-field confirmation of general relativity

A set of weak-field experiments have proven that Einstein's theory of general relativity successfully describes a wide variety of observed phenomena. The first such evidence was given by general relativity's ability to successfully explain the perihelion shift of Mercury and the observed deflection of light passing near the Sun [29].

The perihelion shift of Mercury had been an unresolved problem since 1859 when Le Verrier announced that after accounting for the perturbing effects of the other planets on Mercury's orbit and the precession of the equinoxes, there was still a measurable advance in Mercury's perihelion that could not be explained [29]. Einstein's theory of relativity yielded the first successful explanation of the observed perihelion advance without requiring the introduction of any new physical parameters. This represented a strong argument in favor of general relativity because it proved to be a simple and elegant framework for understanding observed experimental results.

The gravitational bending or lensing of light was proposed as early as 1704 by Newton; however, it was not until 1979 when D. Walsh, R.F. Carswell, and R.J. Weymann detected a double image of a distant quasar. This doubled image was shown to be the result of light from the star being gravitationally lensed around a galaxy [25]. Early classical (non-relativistic) predictions of the amount of light bending due to gravity underestimated the observed angular perturbation by a factor of $\gamma/2$, where γ is the parametrized post-Newtonian parameter measuring the magnitude of space-curvature generated by a unit rest mass [29]. In general relativity, the value of γ is found to be equal to 1 [29]. Einstein's prediction was first verified during a total solar

eclipse following WWI; however, the experiment itself was not particularly accurate, and it was not until the 1960s that more significant evidence could be acquired. Today, high-precision experimental techniques, such as Shapiro time-delay measurements using spacecraft, yield agreement with general relativity to within 0.001 percent [29]. Shapiro time-delays are caused when radio signals are sent past a massive body before being reflected back toward Earth. The gravitational interaction between the light and the massive body induces a time delay that is a function of the signal's closest approach to the Sun.

1.1.2 Strong-field tests of general relativity

Unlike the weak-field limit, the strong-field limit of general relativity has remained largely untested, owing to the difficulty of observing systems in the strong-field regime. Generally, a strong-field system is taken to be one in which a simple first order approximation of the parametrized post-Newtonian framework is no longer appropriate [29]. Such systems contain very massive and dense objects such as black holes and neutron stars. Possibilities for testing general relativity in the strong-field regime involve systems with highly relativistic orbital motions such as late-stage massive inspiralling binary systems. This thesis explores the use of radio astronomy techniques to test general relativity.

Currently, several observational techniques at x-ray wavelengths are being used to probe general relativity in the strong-field regime including spectroscopy and quasi-periodic oscillations in emission intensity. Recently, x-ray spectroscopy has been used to explore the physics of disk accretion in regions near black-holes [23]. Relativistic effects have been found to distort the x-ray spectrum emitted by material accreting onto the black hole. This distortion is a function of black hole parameters such as inclination and spin. Thus, x-ray spectroscopy can be used to constrain these parameters; however, uncertainty in the physics governing accretion near a black hole causes these results to be model-dependent.

Another possibility for studying general relativity in the strong field regime is through quasi-periodic high-frequency x-ray oscillations emitted by stellar-mass black

hole binary systems [20]. In some of these systems, the oscillations exhibit resonances at frequencies which scale as a function of the black hole mass. This relation suggests that general relativity may be able to explain these oscillations; however, scientists have not yet developed a theory to explain these oscillations using general relativity. Therefore it is unclear if general relativity can provide an explanation for this phenomena.

1.2 Testing general relativity using the Event Horizon Telescope

The Event Horizon Telescope (EHT) is a global network of radio telescopes being used simultaneously to observe the environment near the black hole at the galactic center, Sgr A*, with angular resolution on event horizon scales. The goal of this thesis is to use simulation to explore the ability of the EHT to use direct imaging of the black hole to test general relativity in the environment near Sgr A*.

1.2.1 Defining the photon orbit and the black hole shadow

To understand how direct imaging of the region surrounding a black hole might enable tests of general relativity, it is first necessary to understand some key features of a black hole. A black hole is an object whose gravity is so strong that even light is pulled into it. The radius that divides the region in which light can escape the black hole's gravity and that it which light cannot is the black hole event horizon.

The photon orbit is the radius at which photons can stably orbit the black hole. Because photons near the photon orbit will likely orbit the black hole many times before potentially escaping out to the observer, these photons will make a significant contribution to the total disk emission and can be observed as a bright ring near the event horizon using millimeter-wavelength VLBI [1].

The black hole shadow is caused by gravitational lensing of light from sources behind the black hole. Only photons that do not cross the event horizon of the black

hole can be observed by a detector. Furthermore, the probability of such an escape decreases rapidly with proximity to the event horizon. Thus, the scarcity of photons escaping the black hole's gravity to reach the observer from regions near the event horizon creates an observable shadow which, while larger than the actual black hole event horizon, approximately preserves its geometric shape [11].

By observing the black hole shadow and photon ring, strong constraints on the shape of the event horizon can be made. Recent work by Johannsen and Psaltis [18] has shown that the shape of the bright photon ring can be used to investigate any potential deviations in the black hole spacetime from the expected Kerr solution.

1.2.2 The no-hair theorem, the Kerr metric, and perturbations of general relativity

In general relativity the no-hair theorem proves that the spacetimes of black holes are characterized by their masses and spins [18]. This theorem is based on three important assumptions: gravity is really described by general relativity; the black hole is isolated from other significant sources of gravity; and the spacetime is perfectly vacuum outside the black hole [7, 24][1]. While no black hole is perfectly isolated from other sources of gravity and the spacetime is not perfectly vacuum, in realistic astrophysical situations the impact of these deviations from the canonical black hole assumptions is negligible. Therefore, given these assumptions, the no-hair theorem determines that black holes are uniquely characterized by the first two moments of their external spacetimes (i.e. by their mass, M, and spin, J) [18]. All higher order moments can then be defined as a function of M and J (and in units where $G = c = 1$) by:

$$M_l + iS_l = M(ia)^l, \tag{1.1}$$

where $a = J/M$ is the spin parameter and l indexes the order of the moment [18]. The moment M_l describes how matter and energy are distributed in the spacetime, and

[1]Scott Hughes, personal communication, March 28, 2012

moment S_l describes how the flow of matter and energy is distributed [13, 15, 27][2]. Thus, the no-hair theorem can be tested simply by measuring any moments of order greater than two. Any deviation of these higher order moments from the predicted values given by Equation 1.1 will violate the no-hair theorem and demonstrate that the object is not a Kerr black hole.

In their paper, Johannsen and Psaltis [18] parametrize any deviation from the expected quadrupole moment, given by Equation 1.1, with the parameter ϵ and suppose a quadrupole moment, $M_2 \equiv Q$, of the form:

$$Q = -M(a^2 + \epsilon M^2). \tag{1.2}$$

For reasonable distributions of matter near a black hole, ϵ should be zero within general relativity. A non-zero value for ϵ must therefore represent a deviation from general relativity.

1.2.3 Shadow shape as a function of perturbations on general relativity

Johannsen and Psaltis [18] demonstrate how perturbations from general relativity can be observed using VLBI at sub-millimeter wavelengths. In their paper, they consider how the shape of the bright photon ring changes with varying spin, inclination, and deviation from general relativity. The photon ring is a good observable because its shape depends significantly on the black hole spacetime but is not distorted by features in the accretion flow. For Schwarzschild and Kerr black holes in agreement with general relativity, the photon ring is nearly spherical. Any small perturbation from Einsteinian general relativity results in a change in the shape of the photon ring, as shown in Figure 1-1. Nonzero deviations from general relativity can be observed in the oblateness or prolateness of the photon ring. The black hole mass can be measured using the photon ring diameter, and the black hole spin can be measured using the displacement of the centroid of the photon ring from the geometric center of the

[2]Scott Hughes, personal communication, March 28, 2012

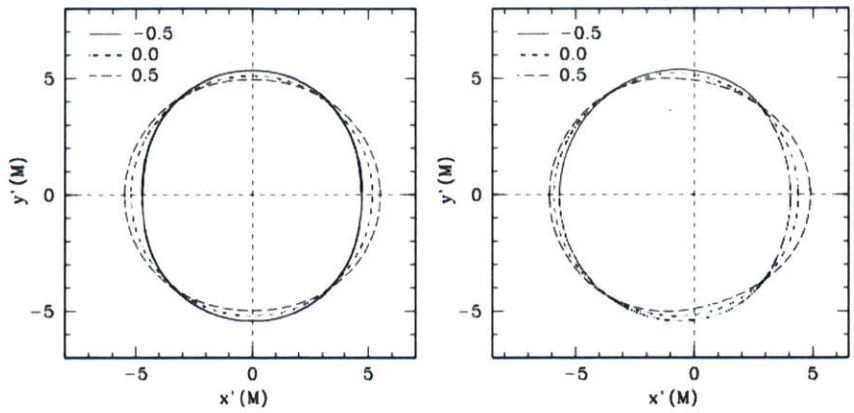

FIGURE 1-1: **Photon ring shape as a function of deviation from general relativity.** This figure shows dependence of photon ring shape on the violation of the no-hair theorem. (Left) corresponds to a zero spin Schwarzschild black hole, while (right) describes a Kerr spacetime with spin parameter $a = 0.4M$. In both cases the observer's inclination is taken to be $\cos(i) = 0.25$. Note how violation of the no-hair theorem causes the shape of the (otherwise circular) photon ring to become ellipsoidal. For a spinning black hole (right) the photon ring exhibits additional asymmetry in cases of nonzero deviation from general relativity. Source: Johannsen and Psaltis [18]

black hole's spacetime. However, this result is not particularly helpful experimentally because of the difficulty of identifying the geometric center of the spacetime from observations. Thus, this work demonstrates imaging to be a powerful tool for probing general relativity in the strong-field regime.

1.2.4 Photon ring radius as a function of black hole mass and spin

The size of the black hole shadow and photon ring are functions of the black hole mass and spin. The photon ring radius, R_p can be expressed as a function of the black hole mass using:

$$R_p = \frac{\sqrt{27}GM}{c^2} \tag{1.3}$$

R_p can also be calculated from an image, using the circle radius given in pixels, the image pixel scale (0.00159 mas/px), and the distance from the observer to the black

hole via:

$$R_p = D_{sgra} \tan(\theta). \tag{1.4}$$

In the above calculation, the black hole is assumed to have spin $a = 0$, for which $R_p = \sqrt{27} R_g$. While R_p depends linearly on the black hole mass, it depends only weakly on spin. For a black hole with spin $a = 1$ the photon ring radius is less than that for a spin $a = 0$ black hole and is given by $R_p = 4.5 R_g$ [5].

The distance to the galactic center, D_{sgra}, is assumed to be 8.3 kpc in the original theoretical models. This value is in agreement with current best estimates of the distance to the galactic center found using observations of the orbital motions of the star S2, known to orbit around the black hole at Sgr A* [14]. Gillessen et al. [14] found $D_{sgra} = 8.28 \pm 0.15|_{\text{stat}} \pm 0.29|_{\text{sys}}$ kpc.

1.2.5 Technological advances necessary to test general relativity

To date 1.3 mm VLBI has been used to observe structure near the event horizon of black holes at Sgr A* and M87, yielding exciting results. In 2008, observations using a 3-station radio telescope array detected structure on scales of $\sim 4\ R_{sch}$, where $R_{sch} = 2GM/c^2$ denotes the Schwarzschild radius of the black hole. These observations also yielded a size estimate for Sgr A* of 36^{+16}_{-10} μas [9]. If the black hole mass and distance from the observer are known, then the angular size of the black hole can be converted to a linear size using:

$$\tan\theta \approx \theta = \frac{R_{sch}}{D_{sgra}} = \frac{2GM}{D_{sgra}c^2}. \tag{1.5}$$

VLBI observations from 2011 have detected time-variable emission on event horizon scales [12]. This growing network of radio telescopes being used to observe Sgr A* comprises the Event Horizon Telescope (EHT).

With current technology, only interferometric amplitudes have been measured. However, with planned increases in array sensitivity in the next few years, inter-

ferometric phase measurements will soon be possible, allowing for the possibility of image reconstruction. Important technological developments require the inclusion of the Atacama Large Millimeter Array (ALMA) as a phased array. This inclusion will increase EHT sensitivity by an order of magnitude and double angular resolution [8]. Furthermore, the addition of new EHT sites in coming years, such as the Plateau de Bure Interferometer (PdBI) and the Institute for Radio Astronomy in the Millimeter Range (IRAM) 30-m telescope, will increase baseline coverage in the (u, v)-plane and allow for greater imaging fidelity, sensitivity, and temporal coverage [8].

Crucial to these efforts is the work laid out in this thesis pertaining to the exploration of imaging algorithms and in testing the ability of VLBI techniques to distinguish between different black hole spacetimes.

Chapter 2

Methods

2.1 Observing astrophysical sources using VLBI

Radio interferometric techniques in astrophysics take advantage of the use of interference patterns to improve angular resolutions beyond those achievable using a single dish [3]. When using a single dish, the angular resolution is a function of both the observing wavelength and the telescope diameter, d [3]:

$$\theta_{min} \sim \frac{\lambda}{d}. \tag{2.1}$$

However, when observing using an interferometric array, the minimum angular resolution decreases with increasing baseline length, allowing for much greater angular resolution:

$$\theta_{min} \sim \frac{\lambda}{B}, \tag{2.2}$$

where B represents the length of the longest baseline in the array [3]. Thus, in the limit of large B, an interferometric array can achieve much greater angular resolution than could be achieved with a single-dish telescope [3]. It is this exceptionally high angular resolution that makes VLBI with the EHT so promising for studying general relativity in the vicinity of the black hole at Sgr A*.

In interferometry, the spatial separation of the telescope antennas causes a geo-

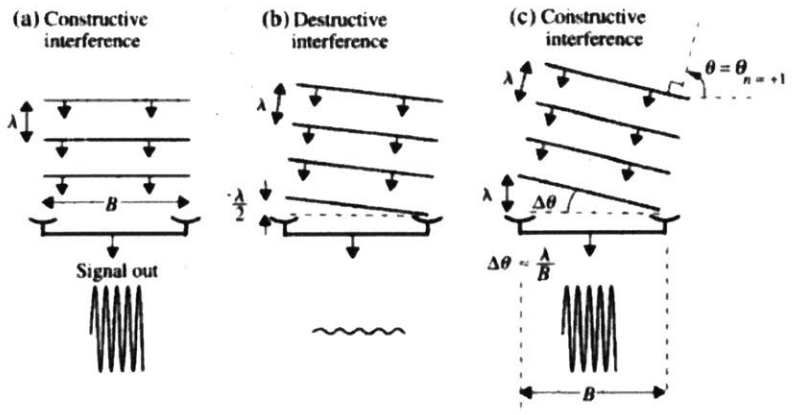

FIGURE 2-1: **A simple two element interferometer.** A diagram of a simple two-element Michelson interferometer. The diagram illustrates how various geometric time delays cause either constructive or destructive interference in the interferometer output signal. Source: Bradt [3]

metric time delay in the reception of signals from a given source (see Figure 2-1). By combining the signals received at both telescopes, the time delay results in points of constructive and destructive interference in the total signal, resulting in a fringe pattern. Information about the brightness distribution of the source necessary for image reconstruction is encoded in the amplitude and phase of this fringe pattern [6].

Because of the periodic nature of the interference response of the array, it is natural to define the response as a complex function having both amplitude and phase, known as the complex visibility function. The complex visibility represents the fundamental observable of radio interferometry [6]. Considering this function in the Fourier or (u, v)-plane, each point in the (u, v)-plane represents interference along a particular baseline at a given time and is a function of the source sky brightness distribution. When successive observations are taken in time, these points begin to trace out curves in the (u, v)-plane, acting to fill in the plane (see Figure 2-2). Interferometric data collected in the Fourier domain can be used to produce images via the inverse Fourier transform; therefore, the (u, v)-coverage of the array directly influences the quality of the reconstructed image.

By the Van Cittert-Zernike Theorem [31], the visibilities are related to the sky brightness distribution by a Fourier transform. With complete sampling of the (u, v)-plane, the image could be reconstructed simply by taking an inverse Fourier transform. Real VLBI arrays, however, only sparsely sample the (u, v)-plane. Mathematically this can be described by multiplying the visibilities by a windowing function whose value is 1 where measurements are obtained and 0 where no data are taken. Since multiplication in one domain becomes convolution in the Fourier conjugate domain, radio astronomers typically produce images by Fourier transforming their visibilities and deconvolving the effects of the widowing function from the dirty image. However, image reconstruction by this method does not necessarily produce a unique image and will fail entirely if the visibility domain is not adequately sampled, as is presently the case for the EHT. Thus, it is necessary to consider alternate imaging algorithms that do not employ deconvolution but are instead based on maximizing the likelihood of the image distribution given the visibility data obtained. One example of such an an algorithm is MACIM, described in §2.3.

Because telescope antennas are so far apart in VLBI arrays, the signals at each telescope are recorded separately and combined after the observation has been completed. Thus, the relative phase between telescopes is unknown and must be recovered during data analysis [6]. Furthermore, for large telescope separations the phase contributions from the Earth's atmosphere may differ at different locations, introducing a random phase difference between the signals received at two antennas. These effects cause instability in the phase of the complex visibility and therefore observations along any single baseline may yield only uncertain information about the sky brightness distribution. The phase information is particularly important because it encodes most of the source structure information [21]. Luckily, when multiple antennas are combined in an array this uncertainty decreases, because the phases around any triangle can be added together in a way which is independent of phase shifts caused by instrumentation or atmospheric effects. This quantity is called the closure phase, ϕ_{ijk} and is given by:

$$\phi_{ijk} = \phi_{ij} + \phi_{jk} + \phi_{ki}, \tag{2.3}$$

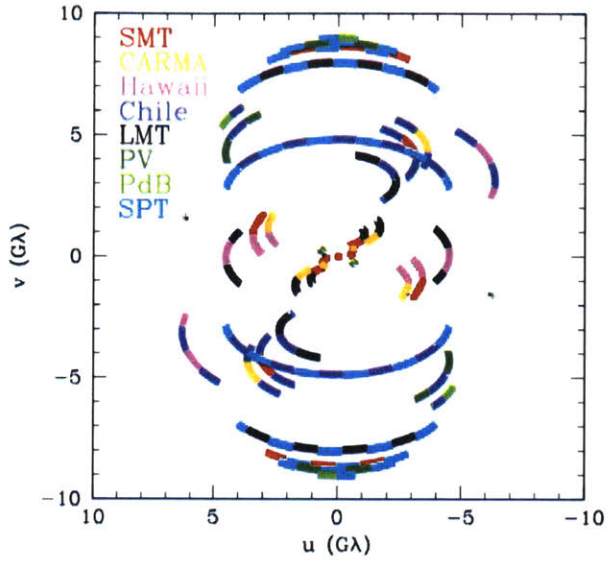

FIGURE 2-2: **(u, v)-coverage of the EHT array used in this thesis.** This figure shows the coverage in the (u, v)-plane for the 8 telescopes used in simulating models of Sgr A*. Each point in the (u, v)-plane represents a Fourier component of the sky brightness distribution. Adapted from: Broderick et al. [4]

for a group of antennas designated i, j and k. The quantity ϕ_{ij} represents the interference phase along the i-j baseline.

2.2 Interstellar scattering and its effect on observation of Sgr A*

Radio waves received from Sgr A* have been observed to be scattered by interstellar plasma (free electrons) along the line of sight between Earth and the galactic center [2]. The effect of this scattering on the observed size of Sgr A* goes as λ^2, and is therefore important at long wavelengths. However, for the purposes of this thesis interstellar scattering effects have been neglected, because at the 1.3 mm wavelengths considered, the measured size is not expected to be dominated by the scattering size [9]. However, this is not necessarily a safe assumption, and scatter broadening effects are expected to be significant on longer baselines. To properly account for interstellar scattering

effects, all theoretical model images should have been convolved with an elliptical gaussian (with parameters in agreement with those produced by interstellar scatter broadening) prior to simulation in MAPS.

2.3 Simulating VLBI observations using MAPS software

As a first step in image reconstruction, it is necessary to create synthetic VLBI data sets from which to attempt a reconstruction. The MIT Array Performance Simulator (MAPS) software, developed by researchers at the MIT Haystack Observatory, is a tool for realistically simulating observations of astrophysical sources with interferometric arrays. The MAPS software uses input information such as a theoretical sky brightness distribution, array geometry, and antenna noise to compute realistic interferometric visibility amplitudes and phases. By using these simulated visibilities it is possible to investigate the ability of the EHT to test general relativity using VLBI observations of Sgr A*.

To successfully accomplish these simulations, theoretical models of the sky brightness distribution around Sgr A* are observed using MAPS. In this thesis, a set of 798 models created by Avery Broderick was sampled to provide the input theoretical sky brightness distributions when running MAPS. These models assume a radiatively inefficient accretion flow (RIAF), meaning that very little of the energy generated during mass accretion by the black hole is radiated away, allowing greater rates of mass accretion to remain in accordance with the observed luminosity of Sgr A* [10]. The spacetime is assumed to be quasi-Kerr, with the ϵ parameter representing deviation from general relativity, as described in the Introduction. The space of all possible models is parametrized in terms of black hole spin parameter, a; inclination angle on the sky, i; orientation angle, θ; and deviation from a Kerr spacetime, ϵ. A sample of one of these input images is given in Figure 2-3.

Additionally, it is necessary to supply information about antenna geometry and

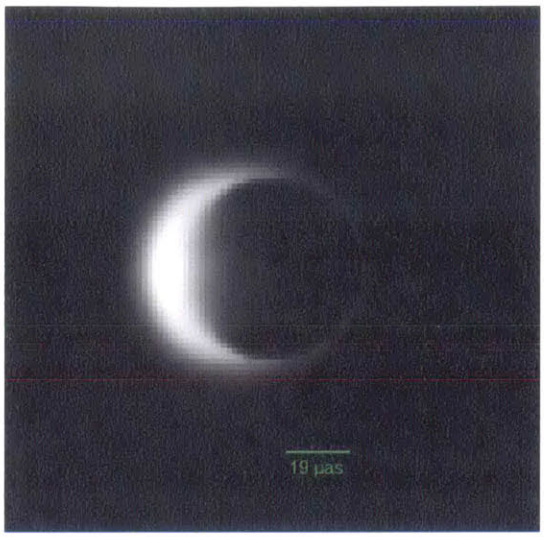

FIGURE 2-3: **A sample image from Broderick's models.** Here the expected black hole shadow and luminous accretion disk are visible. This particular model has $a, i, \epsilon = 0$.

sensitivity (see Table 2.1). For the purposes of radio VLBI, telescope positions are specified using an earth-centered coordinate system (see Figure 2-4 for telescope locations). Antenna sensitivity is input in terms of system equivalent flux density (SEFD), the source flux density necessary to contribute antenna output equal to the system noise of the antenna [26]. Other necessary input includes information regarding the observation itself, such as source right ascension and declination (taken to be the center of the field of view (FOV)), observation start time and duration, channel bandwidth and integration time. In these simulations the observation is assumed to last 24 hours. These values are tabulated in Table 2.2.

Using the input array information, source information, and theoretical sky brightness distribution, MAPS simulates a realistic observation including thermal noise. These data can then be input into image reconstruction software such as MACIM. This process produces an image comparable to what would be obtained if an actual observation was made.

FIGURE 2-4: **Telescope positions of EHT array.** This figure shows the locations of the eight telescopes which comprise the array used in the MAPS simulation.

TABLE 2.1: **Input values for each of the eight telescopes included in the EHT array used in this project.**

Antenna	X (m)	Y (m)	Z (m)	Elev Min(°)	Max	SEFD(Jy)
Hawaii	-5464523.400	-2493147.080	2150611.750	15	85	3300
SMTO	-1828796.200	-5054406.800	3427865.200	15	85	11900
CARMA	-2397431.300	-4482018.900	3843524.500	15	85	7500
LMT	-768713.9637	-5988541.7982	2063275.9472	15	85	4000
ALMA	2225037.1851	-5441199.1620	-2479303.4629	15	85	110
PV	5088967.9000	-301681.6000	3825015.8000	15	85	2900
PdBI	4523998.40	468045.240	4460309.760	10	85	1600
SPT	0.0	0.0	-6359587.3	15	85	10000

TABLE 2.2: **The observation specifications input into MAPS simulations.**

Right Ascension - FOV center	17:45:39.96
Declination - FOV center	-29:00:28.1181
FOV size (arcsec)	0.000159974
Integration time (s)	600.0
Bandwidth (MHz)	500

2.4 Image reconstruction using MACIM

Image reconstruction in the sparse (u, v)-coverage regime is difficult because a large class of images can fit a single interferometric data set [17] since "invisible" sky brightness distributions may be added in regions where the (u, v)-plane is unsampled. The sky brightness distribution in these regions is unconstrained by observation. The MACIM software uses a Monte-Carlo, Markov chain algorithm to find the global minimum of a regularized χ^2 statistic in image space [17]. MACIM uses Bayes' Theorem to calculate the probability of an image being correct given the data set; however, due to the high dimensionality of an image reconstruction problem, it is impossible to evaluate this probability function explicitly. Instead, MACIM takes a statistical approach to sample in only those regions of the total possible image space where the probability is highest.

Re-constructed images are formed from a number of total flux elements, which can be moved between pixels to create new images [17]. There are two ways in which the algorithm considers moving flux elements. The first method is to move a flux element in a random way. If the computed probability for this new arrangement of flux elements is higher than that of the original image, the flux element remains in its new location; if not, the flux element is moved back to its original position. The second method is to introduce new flux elements, or to remove existing flux elements from the image, changing the total number of flux elements present.

Using these stepping techniques, the software iterates though possible arrangements of the flux elements in the image until an image of greatest probability has been identified. There are many different ways of constraining the resulting image, but for the purposes of this project only the standard maximum entropy regularization is considered. Introducing a regularizer acts to constrain the types of images the software looks for. In this thesis, the program was set to search for the most probable solution by maximizing the configurational entropy of the image.

For all models, image reconstruction from simulated MAPS output data was performed using MACIM with the input parameters listed in Table 2.3. Figure 2-5 shows

TABLE 2.3: **Parameters used on all model image reconstructions in MACIM.**

Pixel scale (mas)	0.00159
Image width (px)	100
Entropy multiplier alpha	10
Max (initial) flux elements	5000

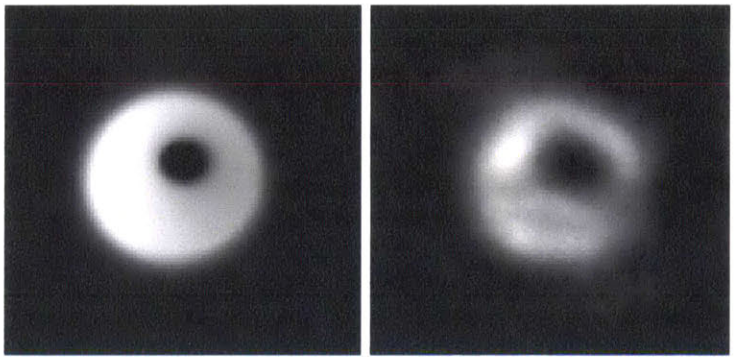

FIGURE 2-5: **Comparing original input models with re-imaged MACIM results.** (Left) The original model used as input for simulations using MAPS. This model has spin parameter $a = 0$, inclination $i = 30°$, and zero deviation from general relativity (i.e. $\epsilon = 0$). (Right) The reconstructed image produced from simulated observation data with realistic thermal noise.

a sample reconstructed image alongside the original theoretical model.

2.5 Fitting for photon ring size using a Hough transform

Following image reconstruction, the size of the photon orbit was extracted using a circular Hough transform. Since size is a function of the black hole mass (see Equation 1.5), this technique allows for direct measurement of the black hole mass. Currently, best estimates of the black hole mass at Sgr A* are provided by the orbital dynamics of stars in close orbits around the black hole as in Gillessen et al. [14]. Since, there may be mass interior to the orbits included in these mass estimates which is not a part of the black hole mass, orbital dynamic techniques can only place an upper

bound on the mass of the black hole. However, it is not unlikely that this mass is negligible compared to the mass of the black hole.

2.5.1 Understanding the Hough transform

The Hough transform was initially developed by Hough in 1962 as a tool for detecting lines in images. It was not until 1975 that Duda and Hart extended the transform to be used for circle detection [19]. The Hough transform can be used to search for a generalized curve in an image, so long as the curve can be expressed as a parametrized equation [16]. To understand the Hough transform, first consider the simple example of line detection.

Following [16], a set of image points, (x, y), which lie on a straight line can be defined by a function, f:

$$f((\hat{m}, \hat{c}), (x, y)) = y - \hat{m}x - \hat{c}, \tag{2.4}$$

where $\hat{m}$ and $\hat{c}$ are the two parameters (slope and intercept) which characterize the line. This relation maps colinear sets of points (x, y) in the image plane to a single point in $(\hat{m}, \hat{c})$ parameter space. The Hough transform considers the parameters of all possible lines which pass through a given image point (x, y). In the linear case, the set of all possible lines passing through each image point define a single line in parameter space as illustrated in Figure 2-6. Using this approach, points which are colinear in image space (i.e. those having the same $\hat{m}$ and $\hat{c}$) intersect at a single common point in parameter space. Since determination of the point of intersection is a local operation rather than a global one, this approach is significantly less computationally intensive than trying to identify the line in the original image space.

The Hough transform reduces the hard problem of shape detection in an image into the comparatively simple problem of vote-counting [16]. The total parameter space is sub-divided into a number of finite-sized regions, which are represented as elements in the accumulator array [16]. Image points vote for all possible parameter combinations that could have produced themselves by incrementing the values in the

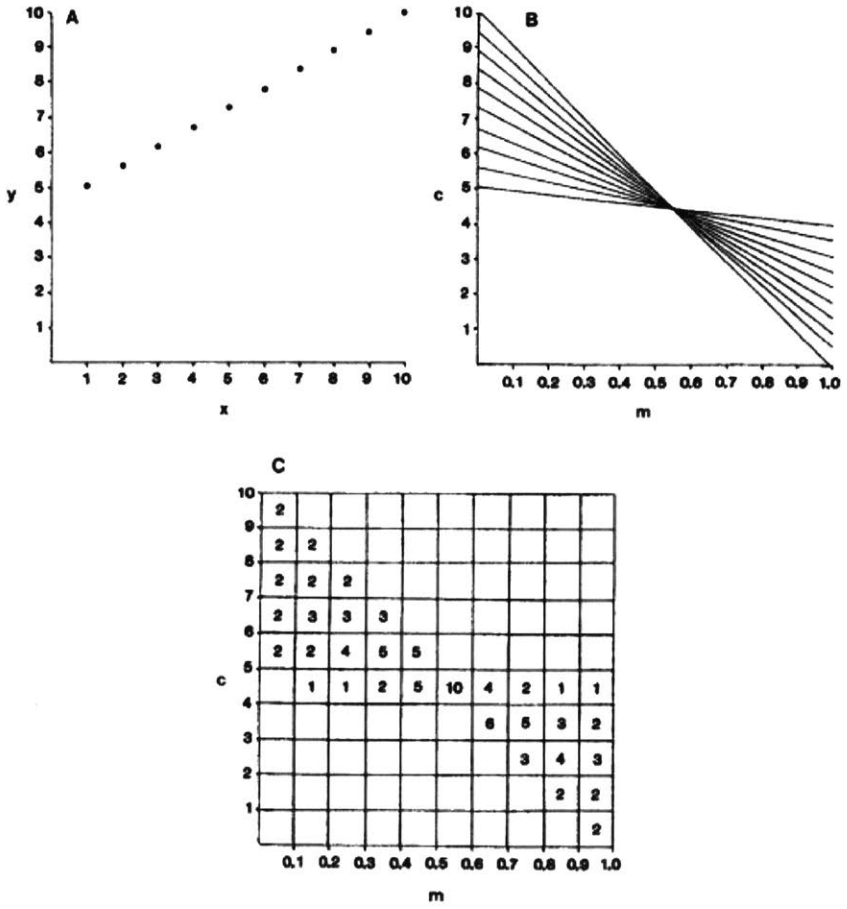

FIGURE 2-6: **Illustrating the Hough transform.** This figure demonstrates the relationship between (A) points in (x, y) image space and (B) their corresponding lines in $(\hat{m}, \hat{c})$ parameter space. (C) Illustrates the accumulator space corresponding to (B). Source: Illingworth and Kittler [16]

accumulator array every time a transformed image point passes through that region of parameter space [16]. After adding up the votes of every point in image space, the totals in the accumulator array indicate the relative likelihood of the shapes being found with the corresponding parameters [16].

2.5.2 Finding circles using the Hough transform

Extending the Hough transform to detect circles is simply a matter of finding a parametrized equation for a circle in terms of the circle center, (x_0, y_0), and its radius, r_0, by the familiar equation [22]:

$$(x - x_0)^2 + (y - y_0)^2 = r_0^2. \tag{2.5}$$

Using this parametrization, each point in parameter space corresponds to the center and radius of a circle or circular arc. A circle in image space corresponds to a right circular cone in parameter space [22]. The common circle between the points on the image plane is then determined by the intersections of the cones in the 3D parameter space.

Prior to the Hough transform, edge detection was performed on the images using the native MATLAB package as follows:

```
edge(im, 'log', 0.0007);
```

where `im` is the input image after being read into MATLAB using `fitsread`. The `'log'` option specifies the Laplacian of Gaussian method of edge detection, and the `0.0007` threshold value was chosen experimentally to appropriately regulate the sensitivity of the edge detection. Edge detection is important because it serves to dramatically decrease the number of points considered in the Hough transform by first identifying which points define shape boundaries.

The edge detection returns a binary image containing only the detected edges, and can be used as input into the Hough transform MATLAB package. In this thesis, the "Hough transform for circles" MATLAB package created by David Young [30] was

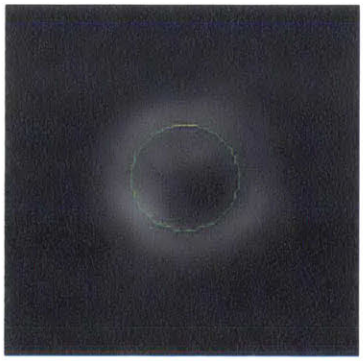

FIGURE 2-7: **An example best circle found using the Hough transform.** The result of using the Hough transform to identify and find the size of the photon ring. The model used has $a = 0$, $i = 30°$, and $\epsilon = 0$.

used to determine the radius of the photon ring in the images resulting from simulation and re-imaging of the theoretical models. The code takes a range of possible radii, which was chosen to be 14-20 px, inclusive. The circle finding code is called with:

```
h = circle_hough(e, radii, 'same', 'normalise');
```

where `e` is the edge-detected image, `radii` is the vector of possible radii, `'same'` forces the code to return only parts of the accumulator array corresponding to circle centers located inside the image, and `'normalise'` scales elements in the accumulator array by $1\backslash R_0$ so as not to weight results in favor of large circles.

After this processing, peaks are found in the accumulator array using:

```
peaks = circle_houghpeaks(h, radii, 'npeaks', 1);
```

where `h` is the accumulator array and `'npeaks'` tells the program to return only the circle with the highest number of counts in the accumulator array. The output `peaks` is a vector containing (x_0, y_0, r_0). An example of the circle returned by this process is shown in Figure 2-7.

2.6 Least-squares fitting of models in the (u, v)-plane

Least-squares model fitting of simulated VLBI data in the (u, v)-plane was also considered as a possible method for gaining traction on general relativity. These fitting techniques represent a non-imaging way of investigating the data and can potentially provide different insights into the ability of the EHT to test general relativity. In this thesis, least-squares fitting of a simple analytical model was investigated.

The model used consists of a circular ring of uniform brightness superimposed with a circular gaussian (see Figure 2-8). This model was chosen because it was expected to be fit high-inclination models well. At high inclinations Doppler-boosting of material orbiting the black hole causes a crescent shape, with a bright region on the approaching side of the accretion disk, and a dim region on the receding side. Thus, a ring+gaussian model, with the added flux due to Doppler-boosting modeled by the gaussian, was thought to be a simple model likely to be well fitted.

2.6.1 Fitting of a ring+gaussian model to simulated datasets

C code developed by Shep Doeleman (MIT Haystack Observatory) and myself uses the simulated VLBI data output from MAPS and compares the simulated visibility amplitude and closure phase data with theoretical data generated from the perfect ring+gaussian model. The χ^2 difference between these two sets of visibilities is then computed. The code searches through a 4D parameter space to determine the best-fitting ring+gaussian model for the MAPS VLBI dataset. Available free parameters are `zsp`, `theta`, `radius`, and `size`, which describe the zero-spacing flux density of the ring, the angle of the gaussian, the inner radius of the ring, and the FWHM of the gaussian, respectively. Because the total flux of the image is constrained to be 2.5 Jy, the zero-spacing flux density parameter really indicates the distribution of flux between the ring and the gaussian in the model.

For the purposes of simplification, the thickness of the ring is fixed as a function

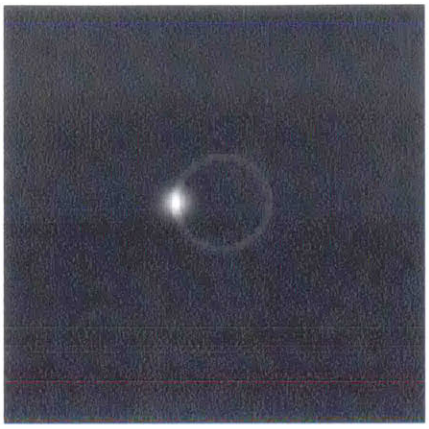

FIGURE 2-8: **Illustrating the ring+gaussian model.** This theoretical model consists of a perfect ring superimposed with a circular gaussian. The free parameters in the model are the brightness of the model, the radius of the ring, the size of the gaussian, and the angle of the gaussian, measured from the right of the image.

of the radius so that the outer diameter of the ring is defined to be `outer = 2.4*R` while the inner diameter is at `inner = 2*R`. The visibilities contributed by the ring are defined by subtracting an inner disk from a larger outer disk. These disks are represented mathematically as Bessel functions given by:

```
disk1 = (2.0/(1-(inner*inner)/(outer*outer)))*zsp*
bessj1(PI*base*outer*4.848e-6)/(PI*base*outer*4.848e-6)
disk2 =(2.0/(1-(inner*inner)/(outer*outer)))*zsp*
((inner*inner)/(outer*outer))*bessj1(PI*base*inner*4.848e-6)/
(PI*base*inner*4.848e-6) ,
```

where `base` = $\sqrt{u^2+v^2}$ and `4.484e-6` converts Mλ*μas to λ*radians. The Bessel function definition used is the standard `bessj1` function taken from Numerical Recipes in C.

The visibilities contributed by the offset circular gaussian are found via:

```
gamp=(2.5-zsp) * exp(-8.367e-11 * base*base*size*size)
gphase =  2.0 * PI * 4.848e-6 * (xg * ulam[i] + yg * vlam[i])  ,
```

where `xg, yg` represent the coordinates of the center of the gaussian (fixed to be in the center of the ring and at an angle `theta`, measured from the right of the image).

From these definitions, the real and imaginary components of the visibilities are computed using:

```
im_vis = gamp * sin(gphase)
re_vis = gamp * cos(gphase) + disk1 - disk2
```

Before the total χ^2 for the visibility amplitudes was calculated, 10% calibration errors were also included:

```
sig_sq_amp = 0.1
*chi_sq_amp += (amp[i] - amp_comp)*(amp[i] - amp_comp)/sig_sq_amp
```

In calculating the χ^2 for the closure phases, a $\sigma = 0.5$ rad was assumed. The difference between the simulated closure phase (from MAPS) and the calculated theoretical closure phases is found by:

```
temp_diff = fmod(cphs[i] - cphs_comp, 2*PI);
if (temp_diff > PI) phase_diff = temp_diff - 2*PI;
else if (temp_diff < -1.0*PI) phase_diff = temp_diff + 2*PI;
else phase_diff = temp_diff;
```

where the `if` statement accounts for appropriate wrapping of the phase around 2π. Once the phase difference has been found, the closure phase contribution to the χ^2 fit is:

```
*chi_sq_cph += phase_diff * phase_diff / sig_sq_cph
```

where `sig_sq_cph = 0.5*0.5` is the assumed uncertainty in the theoretical calculation.

A number of different possible combinations of the available free parameters are tested and the total chi-squared (amplitude and closure phase) is calculated for each. The set of parameters yielding the minimum value of this total chi-squared are returned.

Chapter 3

Results

3.1 Re-imaged models from MACIM

Re-imaged models from MACIM are displayed in Figure A-1. All original model images are included, each with its resulting MACIM output image tiled to the right of the original model in cases where a MACIM result was produced. However, because MACIM only outputs an image if it can find a flux element configuration with a reduced $\chi^2 \leq 1$, not every theoretical model has an associated re-constructed image. If no such image is found, MACIM returns the average of all the flux element distributions considered in its search. These MODE output images often look very little like their original input models (see Figure 3-1) and therefore have been disregarded in all further analysis.

The images in Figure A-1 represent a 133 model swathe through the total 798-model grid. The models given here all have spin $a = 0$; however, all possible inclinations, i, and deviations from general relativity, ϵ, are considered. For these models, the possible inclinations are: $30° \leq i \leq 90°$ in steps of 10°. The possible ϵ considered are: $-0.8 \leq \epsilon \leq 1.0$ in steps of 0.1. This slice through the available parameter space was chosen to test for the ability to differentiate between models with different spacetimes, while controlling for spin and inclination.

In addition to this set of models across ϵ and inclination, a further swathe of 70 models across all spins and inclinations for $\epsilon = 0.4$ was imaged. This set of models

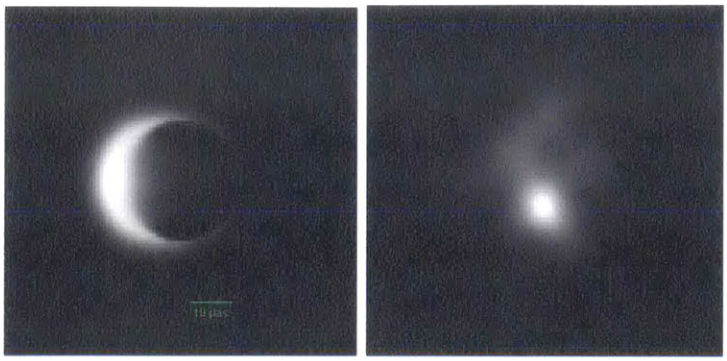

FIGURE 3-1: **Comparing MACIM MODE results with original models.** (Left) The original theoretical model of the black hole sky brightness distribution. (Right) The MODE output from MACIM caused by the program failing to find a brightness distribution with a reduced $\chi^2 \leq 1$. The MODE image is clearly very different from the original model.

was selected because it provided a full range of spins, $0.0 \leq a \leq 0.9$ in steps of 0.1, across all inclinations, but for a single value of ϵ. These models were then used to test for trends as a function of spin. Since the black hole radius is a function of the mass and the spin, this set of models can be used to test for the sensitivity of the methods presented in this thesis to variations in black hole parameters. Plots of these images alongside the original theoretical models are given in Figure A-2.

3.2 Fitted circles using Hough transform

After simulating observations in MAPS and reconstructing images using MACIM, the resulting images were then searched for circles using Hough transform methods. No further analysis was performed on those models for which only a MODE result was produced. The radii of the circles found in images for which MACIM did produce a statistically likely ($\chi^2 \leq 1$) result are tabulated in B.1.

To determine if the Hough transform method could detect deviations from general relativity, circles were found in images with the same spin (here $a = 0$) across all available inclinations, i, and spacetimes, ϵ. To determine if there was any influence of ϵ on the size of the circle fitted, the data were binned at each inclination into regimes

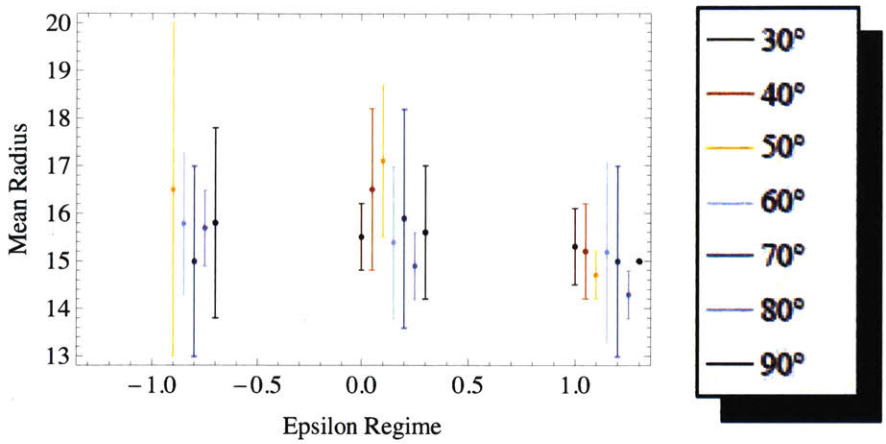

FIGURE 3-2: **Mean Hough transform radius for binned ϵ regimes.** This figure shows the mean and standard deviation of the radii found using the Hough transform after begin binned into regimes of large negative, small, and large positive ϵ. The inclinations have been spread along the ϵ axis to improve readability.

of large negative deviation ($-0.8 \leq \epsilon \leq -0.3$), small deviation ($-0.2 \leq \epsilon \leq 0.4$), and large positive deviation ($0.5 \leq \epsilon \leq 1.0$). In each of these regimes the mean and standard deviation of the circle radii was computed. The results are given in Table C.1 and plotted in Figure 3-2.

Data from the set of images with varying spin and inclination but constant $\epsilon = 0.4$ were also searched for circles using the Hough transform methods. The value of $\epsilon = 0.4$ was chosen because all spins were available at this value of ϵ. The goal of this analysis was to determine if the Hough transform was sensitive to changes in shadow size as a function of black hole spin. Again, the raw data were binned into regions of low spin ($0.0 \leq a \leq 0.4$) and high spin ($0.5 \leq a \leq 0.9$) spin. Data points for which detected circles clearly found part or all of the outer edge of the accretion disk (see Figure 4-1) were excluded to better constrain sensitivity. A mean radius and standard deviation were computed in each bin at each inclination. These results are given in Table C.2 and plotted in Figure 3-3.

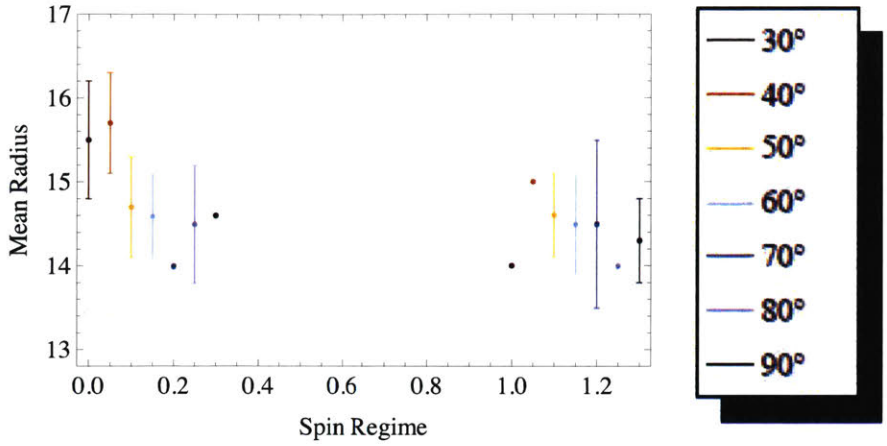

FIGURE 3-3: **Mean Hough transform radius for binned spin regimes.** This figure shows the mean and standard deviation of the radii found using the Hough transform after begin binned into regimes of small and large spin. The inclinations have been spread along the spin axis to improve readability. Points with no error bars have either zero standard deviation or had only one data point in the bin, resulting in an undefined standard deviation.

3.3 Ring+Gaussian least-squares fitting results

Least squares fitting of the simple ring+gaussian model was performed on simulated VLBI amplitude and closure phase data output from MAPS. One advantage of this approach is that because it is a non-imaging technique, it is not dependent upon MACIM finding a statistically good image, but can be performed equally well for any input model.

In this method, an ideal ring+gaussian VLBI dataset is generated and compared with the simulated MAPS output amplitude and closure phase data. The inner radius of the ring, the size of the gaussian, the angle of the gaussian around the ring, and the relative brightness of the gaussian and the ring were fit. Because the technique calculates and compares VLBI amplitude and closure phase data separately, two χ^2 values are returned.

To investigate the sensitivity of this simple model to deviation from general relativity, the ring+gaussian model was first fitted across all inclinations and all spacetimes (all values of ϵ), for for spin $a = 0$. In Figure 3-4, the variation in the χ^2 values from

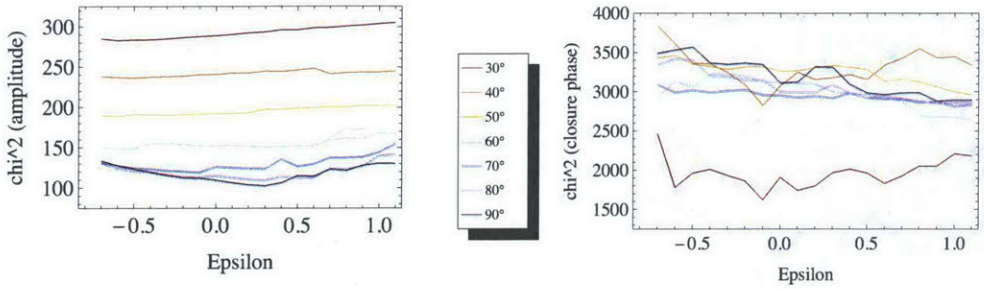

FIGURE 3-4: **Results from ring+gaussian least-squares fitting methods.** Here the χ^2 resulting from fitting VLBI amplitudes and closure phases is plotted against ϵ for all inclinations.

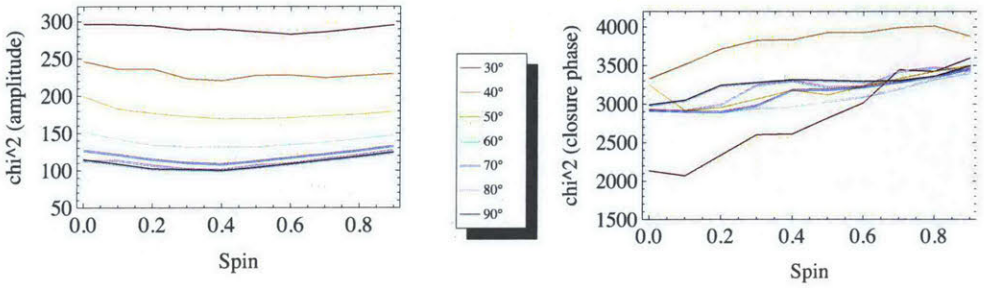

FIGURE 3-5: **Results from fitting using ring+gaussian model for all spins.** Here the χ^2 resulting from fitting VLBI amplitudes and closure phase data is plotted against spin for all inclinations.

fitting the amplitudes and closure phases is plotted as a function of deviation from relativity (ϵ) for all inclinations $30° \leq i \leq 90°$ and for spin $a = 0$.

Next, least-squares fitting was performed across all spins for each inclination at fixed $\epsilon = 0.4$. Again, the value of $\epsilon = 0.4$ was chosen because all spins were available at this value. The resulting χ^2 values are plotted as a function of spin, $0.0 \leq a \leq 0.9$, in Figure 3-5. Plots are included for the χ^2 values resulting from fitting both the VLBI amplitudes and the closure phase data.

In addition to these χ^2 plots, it is instructive to consider the ring radius as a function of both spin and ϵ. These radius plots are given in Figure 3-6 and help to illustrate how sensitive this least-squares fitting approach is to changes in the photon ring size as a function of spin and spacetime.

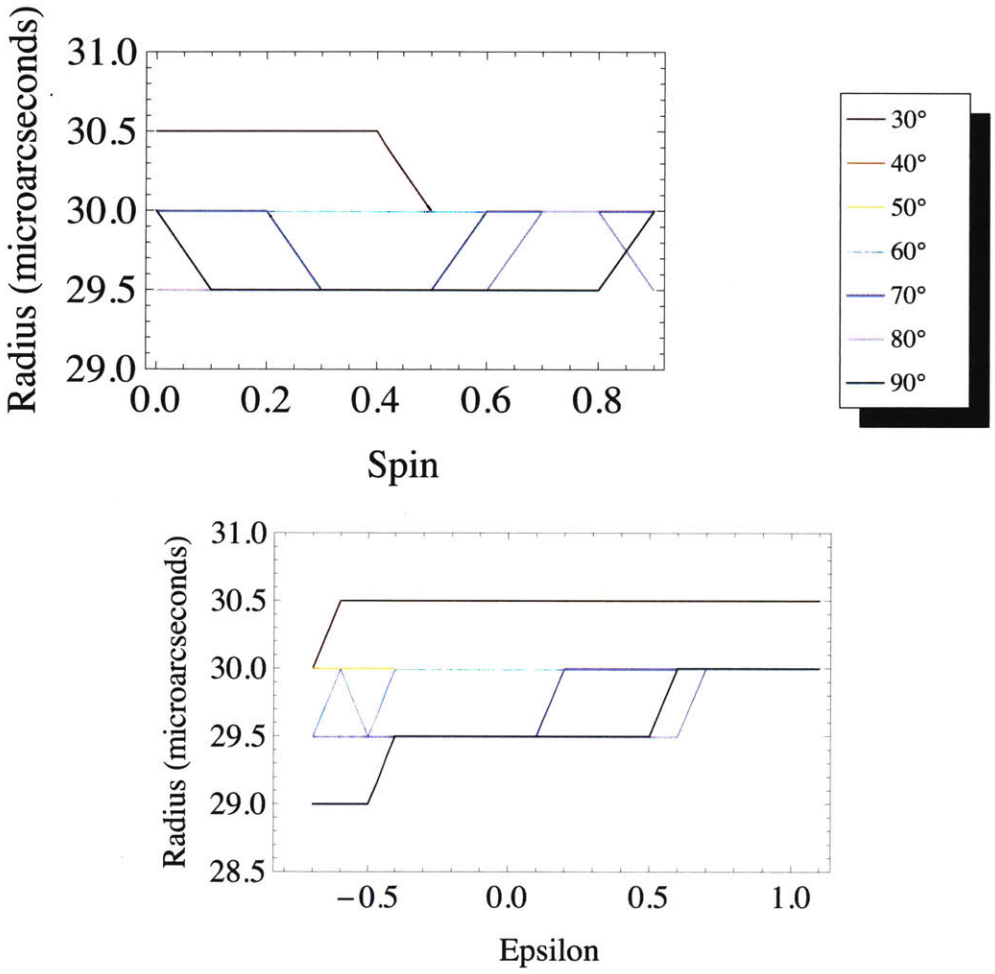

FIGURE 3-6: **Fitted radius as a function of both ϵ and spin using least-squares methods.** (Left) Best-fit radius as a function of spin. (Right) Best-fit radius as a function of ϵ. Note there are no significant trends in the fitted radius as a function of either of these parameters; however, there is some apparent dependence on inclination.

Chapter 4

Analysis

4.1 Analysis of Hough transform data

4.1.1 Determining sensitivity of Hough transform methods to changes in ϵ

To test for sensitivity of the Hough transform method to variations in the value of ϵ, circles were found in the MACIM images and the resulting data were binned into regimes of large negative, small, and large positive deviations from general relativity. The results of this analysis (see Table C.1 and Figure 3-2) show that between the different ϵ regimes, the mean radii in each regime fall within 1σ of each other. This indicates that the Hough transform technique is not sensitive to deviations in general relativity between models with the same spin and inclination.

The likely cause of this insensitivity is two-fold. First, the noise in the data contributes greatly to the error bars and is largely a result of the Hough transform finding all or part of the wrong circle. In a number of cases the Hough transform finds all or part of the outside edge of the accretion disk when searching the image for the best circle. Unfortunately, this renders the resulting circle information useless, as the outer edge of the accretion disk is not related to the black hole parameters. When all or part of the outer edge is detected, circle radii are found to be 18-20 px. This introduces a significant amount of noise into the results. The second difficulty

with the Hough transform technique is that the changes in the shape of the photon ring appear to be below the sensitivity threshold of the method. Because the Hough transform code has only single-pixel resolution and the image is generally fuzzy, the Hough transform is unable to detect any variation in photon ring size or shape as a function of changing ϵ. These issues suggest that a circular Hough transform is not sufficient for resolving changes in ϵ.

4.1.2 Determining spin sensitivity

An investigation into the ability of the Hough transform to detect changes in size of the photon radius as a function of black hole spin was conducted in a similar manner to the test for ϵ sensitivity. However, in this analysis all circle radii which were found to have fitted any part of the outer edge of the accretion disk were eliminated. This was done to prevent these points from anomalously skewing the data, as they had a more significant impact on the smaller spin data sets than they had had in considering the ϵ analysis.

Raw radius data from the Hough transform was binned into regions of high and low spin, and the mean radius and standard deviation was computed. The resulting data given in Table C.2 and plotted in Figure 3-3 show that the Hough transform is not sensitive to differences in photon ring size as a function of spin since mean radii in the high and low spin regimes at every inclination fall within 1σ of each other. However, in every case, except for $i = 70°$, the mean found in the high spin regime is smaller than that found in the low spin regime. While this is in agreement with the expected difference between the two regimes, any potential difference between the two is too small for this method to differentiate between high and low spin regimes with confidence.

TABLE 4.1: **Results of computing the mean and standard deviation of detected circle radii across all ϵ at a given inclination.**

Spin (a)	Inclination (i)	Mean (px)	Std Dev (px)
0	90	15.4	0.7
0	80	15.7	1.4
0	70	16.1	1.9
0	60	15.5	1.6
0	50	15.3	2.0
0	40	14.9	0.8
0	30	15.5	1.4

4.1.3 Black hole mass determination from Hough transform methods

MACIM imaging and Hough transform methods can potentially be used to measure the mass of the black hole directly since the black hole mass is a function of the photon ring radius. To test the ability of these methods in measuring the black hole mass, the mean radius was compared with the radius derived from the known theoretical values input into the original models.aging and Hough transform methods can potentially be used to measure the mass of the black hole directly since the black hole mass is a function of the photon ring radius. To test the ability of these methods in measuring the black hole mass, the mean radius was compared with the radius derived from the known theoretical values input into the original models.

Because the Hough transform method is not sensitive to deviations in ϵ, all ϵ values were subsequently treated together and the mean and standard deviation across all ϵ at each inclination was computed. The results are given in Table 4.1 and show that the average radius found across all inclinations (rounding to the nearest pixel) is 15 px. This result is likely skewed slightly toward larger radii because an examination of the raw data shows that the Hough transform code found at least one circle at every inclination that was all or partially along the outside edge of the disk emission (see Figure 4-1). Thus, the uncertainties could be improved by excluding those data points which clearly fit all or part of the outer edge of the accretion disk. However, even without excluding these data points it is clear that the mean circle radius is

FIGURE 4-1: **An example of the Hough transform finding the outer edge of the accretion disk.** Here the Hough transform has clearly detected the outer edge of the emission for most of the circle. This model has $a = 0$, $i = 70°$, $\epsilon = -0.6$

$\sim$ 15 pixels.

This is interesting because the expected radius for these models can be calculated using the black hole mass and distance to Sgr A* which were assumed in the theoretical models: $D_{sgra} = 8.3$ kpc and $M_{sgra} = 4.5 \times 10^6$ M_{sun} [14][1]. Using these values as input into Equations 1.3 and 1.4, allows the "real" radius of the photon ring to be calculated. Using this approach the photon radius is calculated to be 17.4 pixels, demonstrating that the Hough transform results show a bias toward smaller circle radii.

This discrepancy between the average circle radius and the expected theoretical photon radius can be understood to be a result of the fuzziness of the images. Because the Hough transform is highly sensitive to edges and the emission from the photon ring defines a blurred ring-shaped region, the Hough transform is biased toward finding the innermost edge of this feature. However, the photon ring is actually represented by the circle of maximum brightness in the accretion disk, not the inner edge where the shadow begins. Thus, this technique consistently underestimates the size of the photon radius, resulting in the fitted radius being only about 88% of the expected

[1]Avery Broderick, Personal communication, April 27, 2012

radius.

4.2 Analysis of ring+gaussian fitting results

4.2.1 Testing for goodness of fit

Testing the goodness of fit of the ring+gaussian model to the high-inclination data was performed in two ways. First, a simple reduced χ^2_R was calculated for both the amplitude and closure phase results. This was determined to yield $\chi^2_{R,amp} \approx 0.4 - 1.0$ and $\chi^2_{R,cphs} \approx 5 - 10$. From this we can see that while neither the amplitude or the closure phase fits have the $\chi^2_R \approx 1.0$ that signifies a good fit, the amplitude data is fitted better than the closure phase data. Furthermore, the $\chi^2_{R,amp}$ values are understood, because in assuming 10% calibration errors the error has likely been overestimated, resulting in a $\chi^2_{R,amp} \leq 1.0$. However, the $\chi^2_{R,cphs}$ values are harder to explain and may be indicative of more serious problems with fitting the ring+gaussian model to these high-inclination results.

The problem of goodness of fit can be further tested by plotting the measured flux density as a function of baseline in the (u, v)-plane (see Figure 4-2). This figure shows a discrepancy between the best-fit ring+gaussian model and the simulated VLBI data even at high inclinations, indicating that the ring+gaussian model does not fit well on all baselines even at high inclinations. This is thought to be a result of the gradient brightness in the input model due to Doppler boosting being poorly modeled by the ring+gaussian approximation. A possible solution is to consider an analytical model which can better account for this gradient brightness, as mentioned in §5.1

4.2.2 Understanding the χ^2 trends

Sensitivity of the ring+gaussian least-squares fitting methods to deviations from general relativity can be understood though the best fit χ^2 values. The same set of models were used as in the Hough transform analysis, sampling across all ϵ at each inclination for spin $a = 0$. This allows changes in the χ^2 values as a function of ϵ to

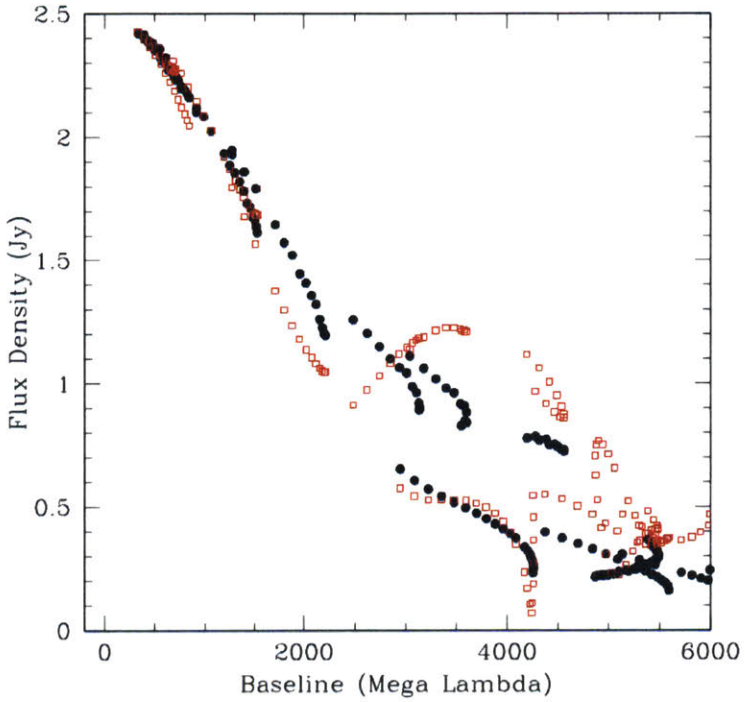

FIGURE 4-2: **Comparing flux density vs. baseline for the best ring+gaussian model and the the simulated VLBI data.** Here the best-fit ring+gaussian model is plotted in red, and the simulated VLBI data in black. The discrepancy between the red and black curves indicate that the ring+gaussian model does not fit well on all baselines even at high inclinations.

be observed when plotted (see Figure 3-4). Understanding the trends in χ^2 as a function of ϵ helps to explain the ability of least-squares fitting techniques to differentiate between models with different ϵ values.

There are several trends worth considering in the χ^2 plots of Figures 3-4 and 3-5. First, consider the $\chi^2_{\rm amp}$ plots as a function of ϵ. Looking at the value of $\chi^2_{\rm amp}$ across all inclinations demonstrates that the high-inclination models ($i \geq 70°$) are better fit by the ring+gaussian model than low-inclination models. This is unsurprising because the original low-inclination models look very little like a ring+gaussian. Additionally, for these high-inclination models the $\chi^2_{\rm amp}$ as a function of ϵ shows a decrease in regions of small ϵ. This dip seems to suggest that the $\chi^2_{\rm amp}$ may be sensitive to deviations from the expected circular shape of the model ring. However, to get a clear indication of the significance of this change in $\chi^2_{\rm amp}$ ($\delta\chi^2_{\rm amp} \approx 30$), it would be important to re-calculate the reduced χ^2 after more properly estimating the expected calibration errors. This would help to determine if the ring+gaussian models are fitting well, and how much statistical significance to assign to the feature. Clearly this dip does not appear at lower inclinations for the ring+gaussian model, but it is possible that a new analytical model could be developed that would be similarly sensitive at lower inclinations. Unfortunately, there is no similar trend in $\chi^2_{\rm cphs}$ as a function of ϵ; instead, $\chi^2_{\rm cphs}$ seems to decrease only slightly as ϵ increases. This is potentially problematic because visibility amplitudes can only be calibrated to within a few percent. Therefore, any test that depends sensitively on fitting the amplitude data may be inconclusive when used on real VLBI data. However, this may be an indication that considering closure amplitudes (an amplitude quantity independent of atmospheric effects akin to the closure phase which can be defined between any 4 telescopes in an array) may be fruitful in constraining the observed black hole spacetime.

The χ^2 data as a function of black hole spin exhibits the opposite behavior. In this case, $\chi^2_{\rm cphs}$ demonstrates a clear increase with increasing spin, while $\chi^2_{\rm amp}$ remains nearly constant as a function of spin. Thus, the phase information seems to be most important in differentiating between models with different spins using least-squares

fitting, and could indicate the potential for differentiating between models of different spins using closure phases.

4.2.3 Determining black hole mass from ring+gaussian fitting

Considering only those high-inclination ($i \geq 70°$) models for which the ring+gaussian model seems to fit better, the mean radius across all ϵ at zero spin is between 29.5 and 30 μas. Using the same calculations for the photon ring size as a function of black hole mass at zero spin as in §4.1.3 (Equations 1.3 and 1.4), the theoretical radius of the photon ring is calculated to be 27.9 μas. Thus, the least-squares fitting technique appears to slightly over-estimate the size of the photon ring, unlike the Hough transform methods which were found to underestimate the radius. The least-squares fitting methods more correctly identify the size of the photon ring, with only 5-7% error, as opposed to the 22% discrepancy found when using the Hough transform methods. It is possible that the ring+gaussian model does a more accurate job of fitting for the size of the photon ring because of the fixed width of the ring in the model. The fixed width could cause the best fit to occur when the brightest part of the accretion disk is found within the model ring.

4.2.4 Determining sensitivity to photon ring size as a function of black hole spin

Based on the ring+gaussian fitting results given in Figures 3-5 and 3-6, there does not appear to be any evidence to indicate sensitivity to changing photon ring size as a function of black hole spin. The plot in Figure 3-6 as a function of spin is particularly compelling, as it shows no evidence of the expected decreasing trend. Instead, the plots show that the fitted radius does not depend on either spin or ϵ, while the radius does seem to depend somewhat on inclination. This dependence on inclination is likely the result of the ring+gaussian model being a poor approximation at low inclinations. Therefore, it must be concluded that the ring+gaussian least squares

fitting technique is unable to differentiate between models with different black hole spins by fitting for the radius of the photon ring.

Chapter 5

Discussion

This thesis explores the feasibility of testing general relativity in the strong-field regime using millimeter wavelength VLBI of Sgr A*. Using theoretical models and simulating realistic VLBI observations with MAPS allows for the creation of VLBI datasets which can be used to explore techniques for testing relativity. Both imaging and non-imaging techniques are considered to determine if non-imaging methods are more or less effective than imaging techniques in constraining black hole parameters such as spin and spacetime.

5.1 Summary of important results

Image reconstruction from the VLBI data was performed using statistical algorithms in MACIM. The resulting images were then analyzed using a Hough transform to identify the best circle in each image. This approach proved to be largely unsuccessful in constraining black hole parameters such as spin and ϵ. The technique also showed consistent bias with radii found to be on average 22% smaller than the expected photon ring radius. This result was attributed to the blurred quality of the image. Nevertheless, if the bias were well characterized, this method could perhaps be used to measure the black hole mass directly using millimeter wavelength VLBI.

The non-imaging technique considered in this thesis uses least-squares fitting of a simple parametrized ring+gaussian model to the raw VLBI amplitude and closure

phase data in the (u, v)-plane. Analysis of the method concludes that the simple ring+gaussian model is not a great approximation to the structure of the accretion disk even at high inclinations ($i \geq 70°$), possibly due to the gradient brightness of the disk emission caused by Doppler boosting. Thus, further study of least-squares techniques should develop new analytical models that work well all inclinations. One possible model is a ring of gradient brightness, were flux is distributed across the ring in a linear or quadratic manner. The development of new analytical models is particularly necessary in light of analysis of the most recent VLBI data which indicates the most probable values of the black hole parameters to be $a = 0.0^{+0.64+0.85}$ and $\theta = 68^{\circ}{}^{+5^{\circ}+9^{\circ}}_{-20^{\circ}-28^{\circ}}$ [4]. Thus, high inclination models are not favored by existing VLBI data from past observations of Sgr A*.

The χ^2_{amp} data plotted against ϵ seems to indicate that the least-squares fitting techniques may be sensitive to deviations from circularity of the photon ring in high-inclination cases were the accretion disk emission is most similar to the analytical model. Although visibility amplitudes may be difficult to calibrate precisely enough to detect non-circularity in the shape of the photon ring, closure amplitudes, which are robust against calibration uncertainties, may be a promising substitute in future investigations. Thus, further research is necessary to determine if the observed change in χ^2_{amp} as a function of ϵ can be used to constrain the black hole spacetime. Although the ring+gaussian model is unable to distinguish between large positive and large negative deviations from general relativity, it is possible that this least-squares fitting approach could be developed into a tool for distinguishing between these regimes. This would be an exciting result which could enable observers to constrain possible deviations from general relativity using VLBI observations of Sgr A*.

The least-squares fitting approach proves to be more reliable than the Hough transform in measuring photon ring size. This is possibly because parameters which place the brightest part of the accretion disk inside the model ring are statistically favored, rather than the transition from shadow to disk emission which appears to be favored using the Hough transform. With results only 5-7% larger than the expected radius for high-inclination cases in which the ring+gaussian model does well, this

method does considerably better than the 22% underestimate found using the Hough transform. Neither method appears to be able to detect changes in the photon ring size as a function of black hole spin.

5.2 Possibilities for future work

Based on these results of this thesis, there are several areas for future work. This work has demonstrated the existence of trends in χ^2 as a function of black hole parameters which could potentially be exploited to study general relativity near Sgr A*. More investigation is required to determine if the magnitude of these trends is significant as well as to develop better analytical models for least-squares fitting of theoretical models. These analyses will determine if changes in photon ring shape as a function of the black hole spacetime can be constrained using least-squares fitting.

Additionally, while the circular Hough transform methods considered in this thesis proved to be largely unsuccessful in extracting black hole parameters, it is not unlikely that there exist other imaging methods for investigating black hole parameters. Therefore, it is worthwhile to continue to explore techniques for extracting black hole parameters from simulated and re-imaged models of Sgr A*. Possibilities for such exploration include an elliptical Hough transform or a different shape-detection algorithm.

Another important consideration for future work is interstellar scattering. While interstellar scattering was not considered in this study, it is expected to have an effect on the results, and a truly realistic simulation of VLBI observations of Sgr A* would need to properly account for these effects.

5.3 Conclusions

The opportunity to observe the black hole at Sgr A* on event horizon scales using millimeter wavelength VLBI represents an unprecedented opportunity to study general relativity in the strong field limit. The work done in this thesis represents a first

attempt at using new imaging and non-imaging different techniques to constrain the black hole parameters based on realistic simulations of VLBI observations. Previous research in this area has focused on using exiting VLBI data from observations of Sgr A* to place bounds on the black hole parameters. This thesis seeks to identify to constrain the full potential of the EHT for extracting black hole parameters. These results demonstrate the promise of such an approach and indicate several directions for future work.

Appendix A

Original and MACIM output images

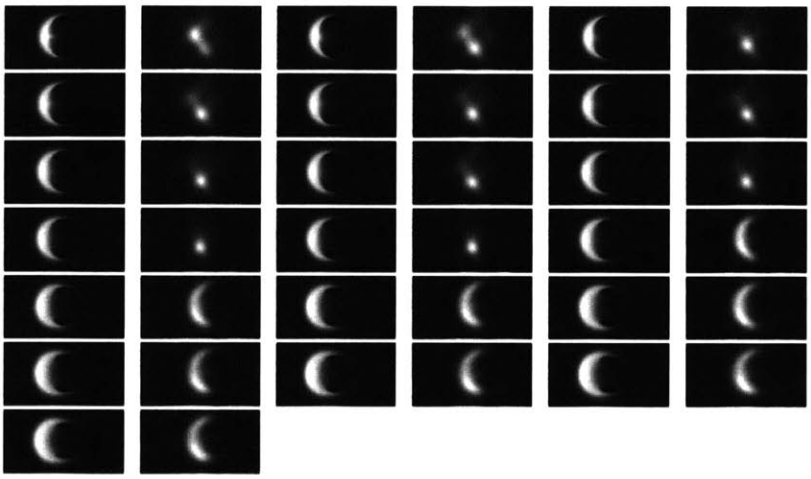

(a) Models with $a = 0, i = 90°$, $-0.8 \leq \epsilon \leq 1.0$ in steps of 0.1 from left to right

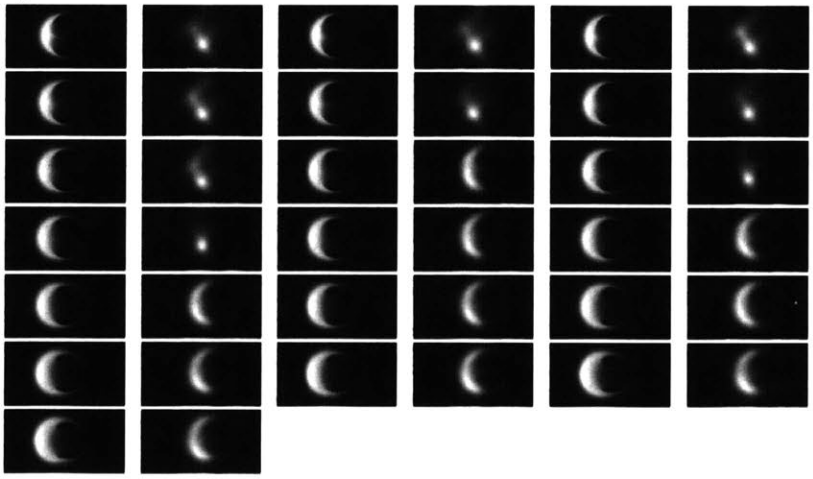

(b) Models with $a = 0, i = 80°$, $-0.8 \leq \epsilon \leq 1.0$ in steps of 0.1 from left to right

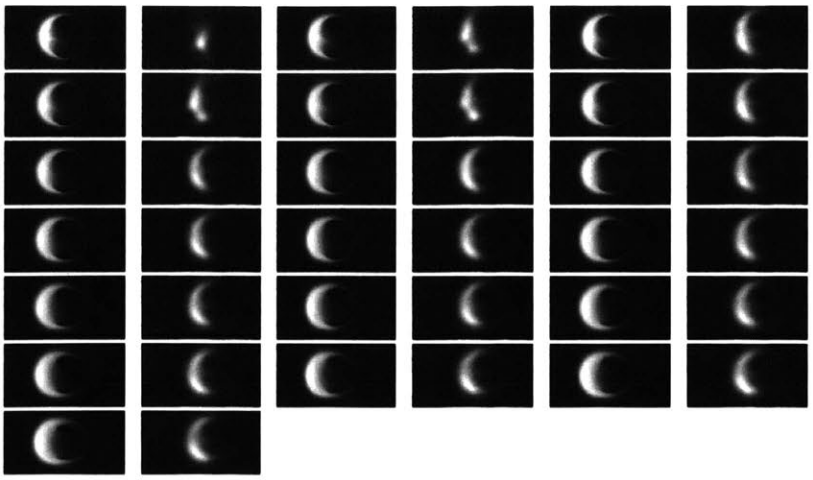

(a) Models with $a = 0, i = 70°$, $-0.8 \leq \epsilon \leq 1.0$ in steps of 0.1 from left to right

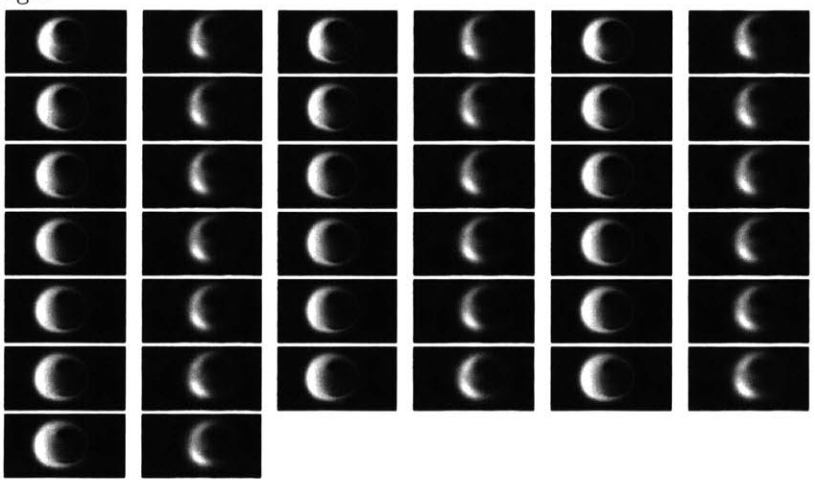

(b) Models with $a = 0, i = 60°$, $-0.8 \leq \epsilon \leq 1.0$ in steps of 0.1 from left to right

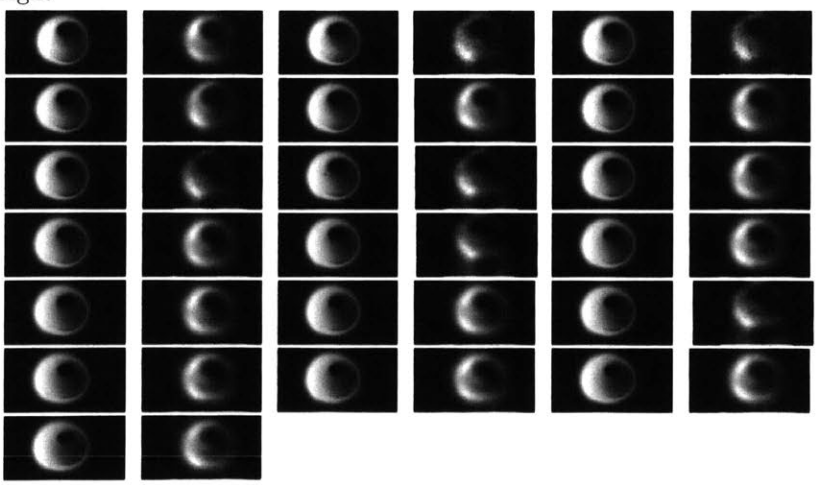

(c) Models with $a = 0, i = 50°$, $-0.8 \leq \epsilon \leq 1.0$ in steps of 0.1 from left to right

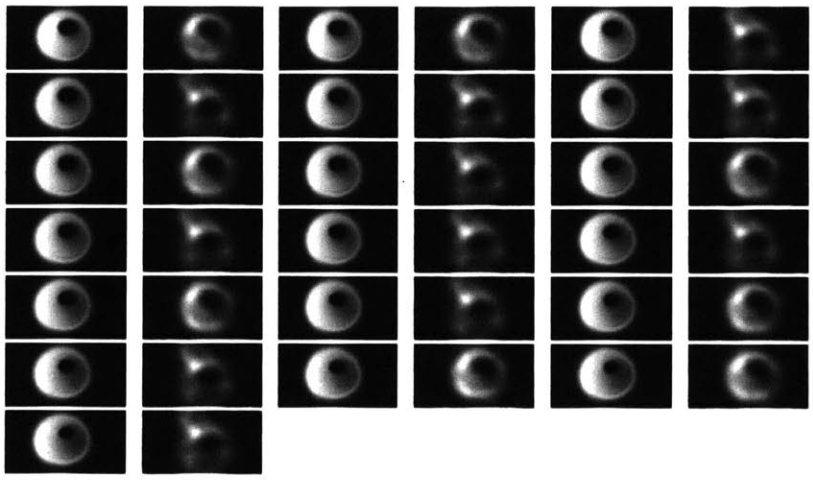

(a) Models with $a = 0, i = 40°$, $-0.8 \leq \epsilon \leq 1.0$ in steps of 0.1 from left to right

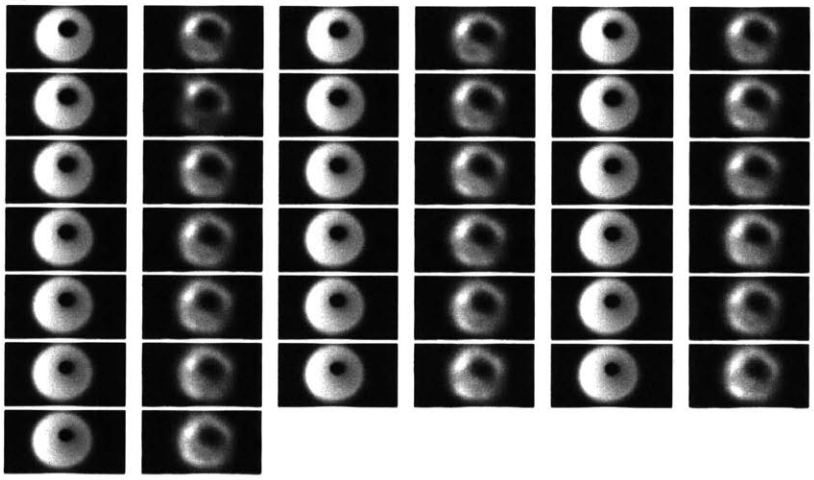

(b) Models with $a = 0, i = 30°$, $-0.8 \leq \epsilon \leq 1.0$ in steps of 0.1 from left to right

FIGURE A-1: **Theoretical models vs. MACIM results for all inclinations and ϵ.** Here the re-imaged MACIM output images are shown to the right of their corresponding theoretical model. In a few cases, when MACIM was unable to produce a suitable reconstructed image, the MODE output image is printed.

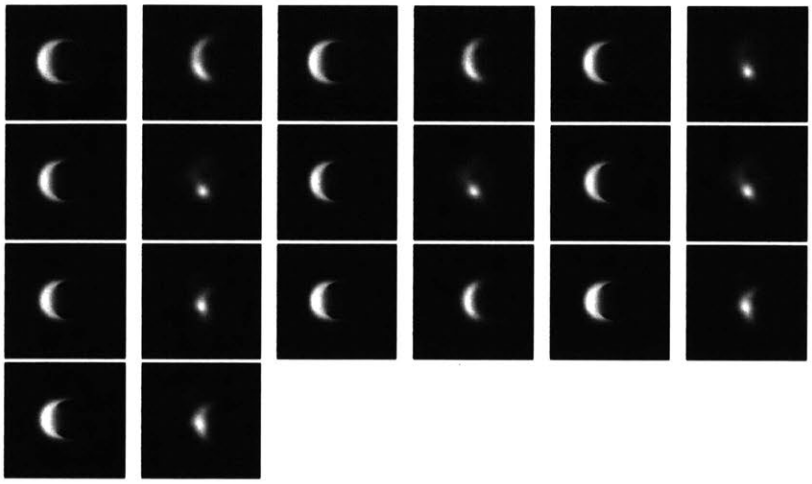

(a) $0.0 \leq a \leq 0.9$ in steps of 0.1 from left to right, $i = 90°$, $\epsilon = 0.4$

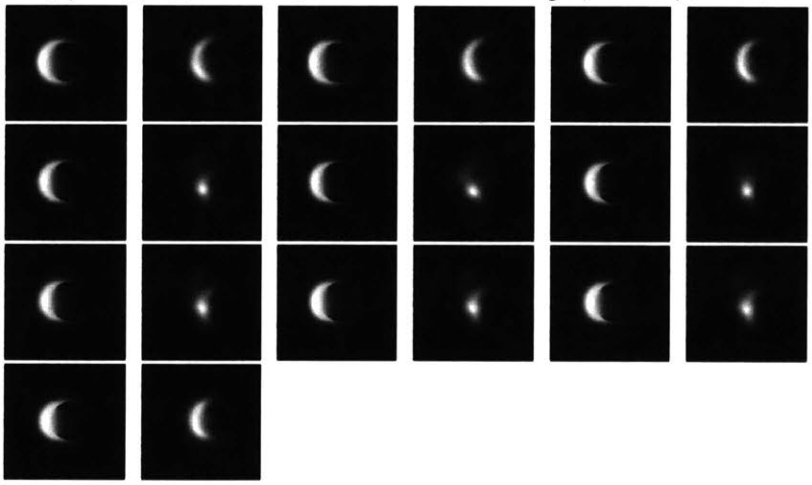

(b) $0.0 \leq a \leq 0.9$ in steps of 0.1 from left to right, $i = 80°$, $\epsilon = 0.4$

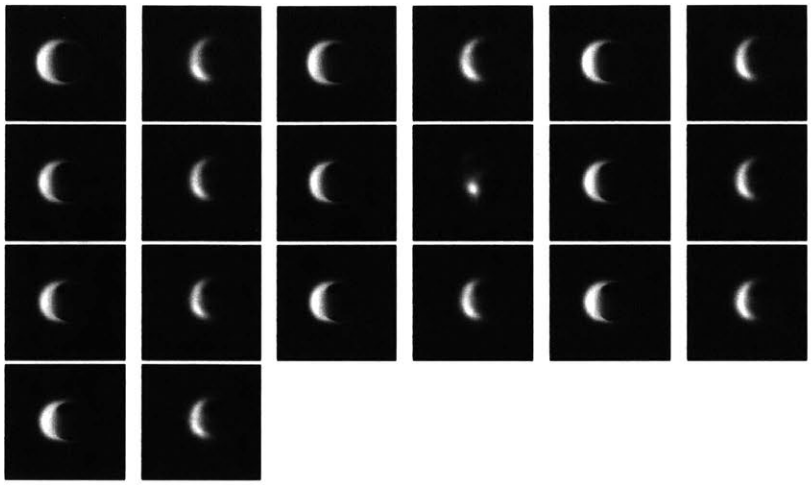

(a) $0.0 \leq a \leq 0.9$ in steps of 0.1 from left to right, $i = 70°$, $\epsilon = 0.4$

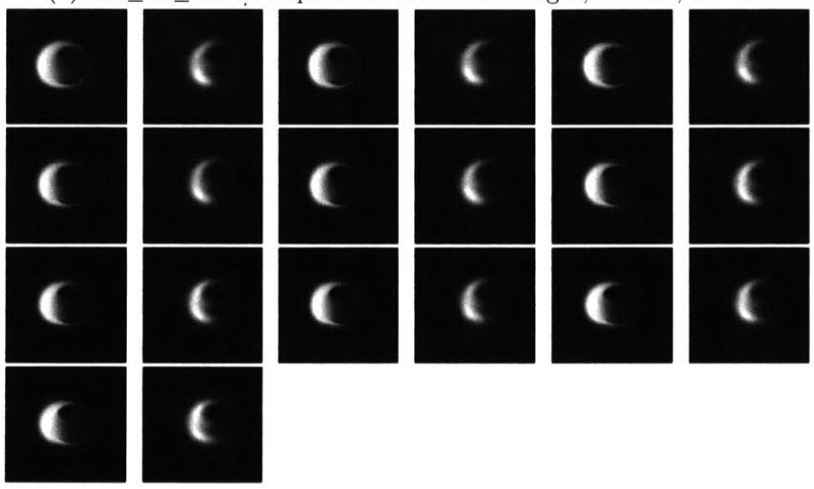

(b) $0.0 \leq a \leq 0.9$ in steps of 0.1 from left to right, $i = 60°$, $\epsilon = 0.4$

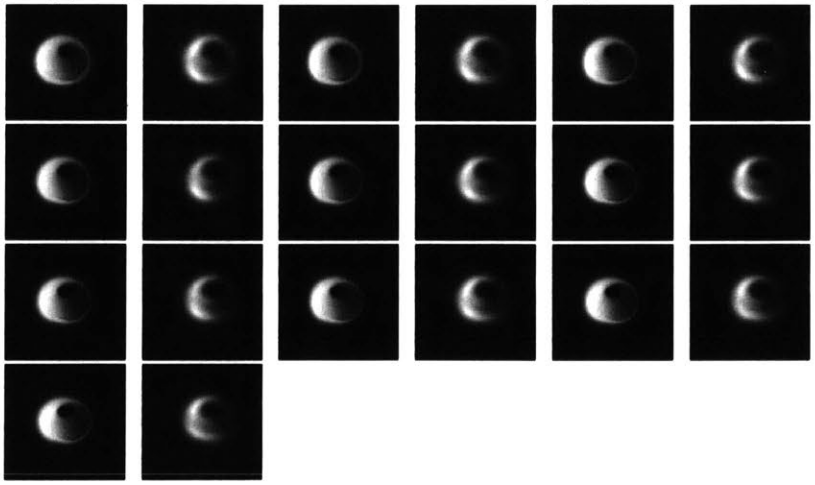

(c) $0.0 \leq a \leq 0.9$ in steps of 0.1 from left to right, $i = 50°$, $\epsilon = 0.4$

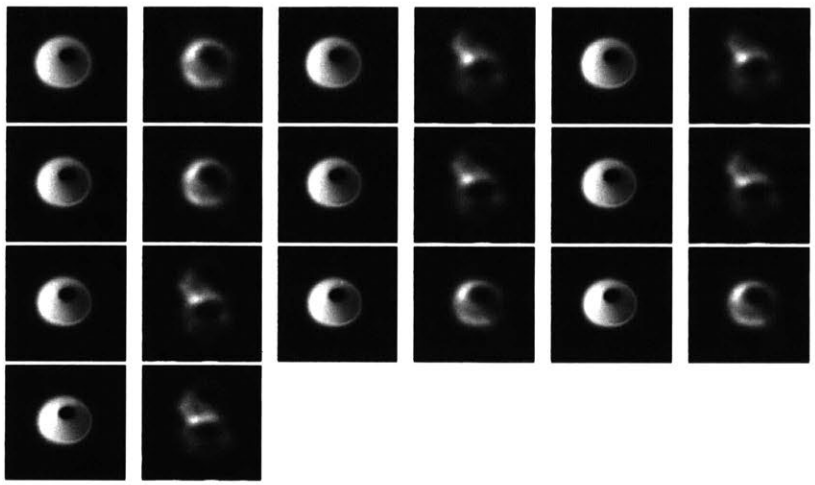

(a) $0.0 \leq a \leq 0.9$ in steps of 0.1 from left to right, $i = 40°$, $\epsilon = 0.4$

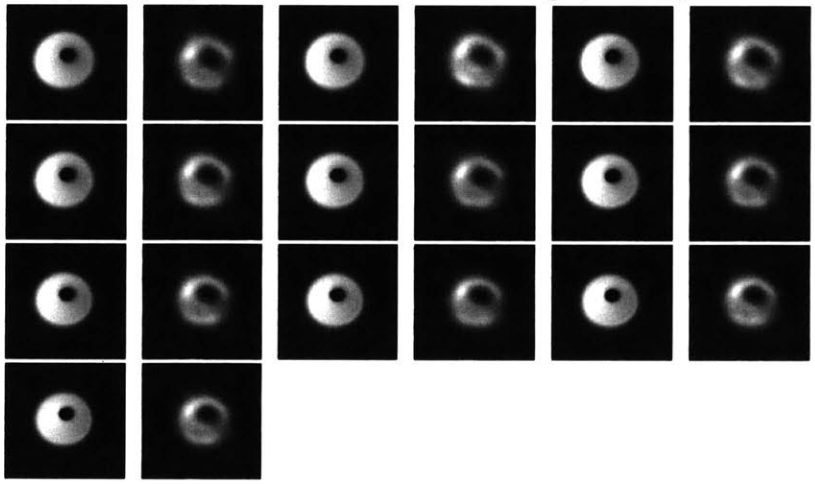

(b) $0.0 \leq a \leq 0.9$ in steps of 0.1 from left to right, $i = 30°$, $\epsilon = 0.4$

FIGURE A-2: **Theoretical models vs. MACIM results for all inclinations and spins.** Here the re-imaged MACIM output images are shown to the right of their corresponding theoretical model. In a few cases, when MACIM was unable to produce a suitable reconstructed image, the MODE output image is printed.

Appendix B

Raw data from finding circles using the Hough transform

Recall, the pixel scale of the images is 0.00159 mas/pixel. The assumed mass of and distance to Sgr A* are taken to be: $M_{sgra} = 4.5 \times 10^6$ M_{sun} and $D_{sgra} = 8.3$ kpc.

TABLE B.1: **Data from finding circles in MACIM images using the Hough transform.**

Spin (a)	Inclination (deg)	GR Deviation (ϵ)	Circle Radius (px)
0	90	0.3	15
0	90	0.4	16
0	90	0.5	15
0	90	0.6	15
0	90	0.7	15
0	90	0.8	15
0	90	0.9	17
0	90	1.0	15
0	80	-0.1	16
0	80	0.2	16

Continued on next page

TABLE B.1 – continued from previous page

Spin (a)	Inclination (deg)	GR Deviation (ϵ)	Circle Radius (px)
0	80	0.3	15
0	80	0.4	19
0	80	0.5	15
0	80	0.6	16
0	80	0.7	15
0	80	0.8	15
0	80	0.9	17
0	80	1.0	14
0	70	-0.6	19
0	70	-0.3	14
0	70	-0.2	18
0	70	-0.1	17
0	70	0.0	19
0	70	0.1	18
0	70	0.2	15
0	70	0.3	18
0	70	0.4	15
0	70	0.5	15
0	70	0.6	15
0	70	0.7	15
0	70	0.8	14
0	70	0.9	15
0	70	1.0	14
0	60	-0.8	18
0	60	-0.7	15
0	60	-0.6	14

Continued on next page

TABLE B.1 – continued from previous page

Spin (a)	Inclination (deg)	GR Deviation (ϵ)	Circle Radius (px)
0	60	-0.7	17
0	60	-0.4	15
0	60	-0.3	16
0	60	-0.2	19
0	60	-0.1	15
0	60	0.0	15
0	60	0.1	14
0	60	0.2	15
0	60	0.3	15
0	60	0.4	15
0	60	0.5	15
0	60	0.6	14
0	60	0.7	15
0	60	0.8	19
0	60	0.9	14
0	60	1.0	14
0	50	-0.8	14
0	50	-0.7	14
0	50	-0.6	14
0	50	-0.5	15
0	50	-0.4	19
0	50	-0.3	14
0	50	-0.2	14
0	50	-0.1	15
0	50	0.0	14
0	50	0.1	19

Continued on next page

TABLE B.1 – continued from previous page

Spin (a)	Inclination (deg)	GR Deviation (ϵ)	Circle Radius (px)
0	50	0.2	16
0	50	0.3	19
0	50	0.4	14
0	50	0.5	14
0	50	0.6	15
0	50	0.7	14
0	50	0.8	19
0	50	0.9	14
0	50	1.0	14
0	40	-0.8	15
0	40	-0.7	15
0	40	-0.6	16
0	40	-0.5	16
0	40	-0.4	17
0	40	-0.3	15
0	40	-0.2	15
0	40	-0.1	15
0	40	0.0	15
0	40	0.1	14
0	40	0.2	15
0	40	0.3	16
0	40	0.4	14
0	40	0.5	14
0	40	0.6	15
0	40	0.7	14
0	40	0.8	14

Continued on next page

TABLE B.1 – continued from previous page

Spin (a)	Inclination (deg)	GR Deviation (ϵ)	Circle Radius (px)
0	40	0.9	15
0	40	1.0	14
0	30	-0.8	15
0	30	-0.7	15
0	30	-0.6	15
0	30	-0.5	20
0	30	-0.4	15
0	30	-0.3	15
0	30	-0.2	15
0	30	-0.1	19
0	30	0.0	15
0	30	0.1	15
0	30	0.2	15
0	30	0.3	15
0	30	0.4	15
0	30	0.5	15
0	30	0.6	15
0	30	0.7	15
0	30	0.8	15
0	30	0.9	15
0	30	1.0	15
0.0	90	0.4	16
0.1	90	0.4	15
0.7	90	0.4	14
0.0	80	0.4	15
0.1	80	0.4	16

Continued on next page

TABLE B.1 – continued from previous page

Spin (a)	Inclination (deg)	GR Deviation (ϵ)	Circle Radius (px)
0.2	80	0.4	16
0.9	80	0.4	19
0.0	70	0.4	15
0.1	70	0.4	15
0.2	70	0.4	18
0.3	70	0.4	15
0.5	70	0.4	15
0.6	70	0.4	15
0.7	70	0.4	19
0.8	70	0.4	18
0.9	70	0.4	14
0.0	60	0.4	15
0.1	60	0.4	14
0.2	60	0.4	15
0.3	60	0.4	15
0.4	60	0.4	14
0.5	60	0.4	15
0.6	60	0.4	17
0.7	60	0.4	14
0.8	60	0.4	14
0.9	60	0.4	15
0.0	50	0.4	14
0.1	50	0.4	14
0.2	50	0.4	19
0.3	50	0.4	14
0.4	50	0.4	20

Continued on next page

TABLE B.1 – continued from previous page

Spin (a)	Inclination (deg)	GR Deviation (ϵ)	Circle Radius (px)
0.5	50	0.4	14
0.6	50	0.4	18
0.7	50	0.4	14
0.8	50	0.4	14
0.9	50	0.4	16
0.0	40	0.4	15
0.1	40	0.4	18
0.2	40	0.4	14
0.3	40	0.4	19
0.7	40	0.4	19
0.8	40	0.4	14
0.0	30	0.4	17
0.1	30	0.4	15
0.2	30	0.4	15
0.3	30	0.4	14
0.4	30	0.4	18
0.5	30	0.4	14
0.6	30	0.4	15
0.7	30	0.4	14
0.8	30	0.4	14
0.9	30	0.4	17

Appendix C

Binned Hough transform data

TABLE C.1: **Results of binning data into regimes of small, large positive, and large negative ϵ.**

Spin (a)	Inclination (i)	ϵ Regime	Mean (px)	Std Dev (px)
0	90	small	15.5	0.7
0	90	pos	15.3	0.8
0	80	small	16.5	1.7
0	80	pos	15.2	1.0
0	70	neg	16.5	3.5
0	70	small	17.1	1.6
0	70	pos	14.7	0.5
0	60	neg	15.8	1.5
0	60	small	15.4	1.6
0	60	pos	15.2	1.9
0	50	neg	15.0	2.0
0	50	small	15.9	2.3
0	50	pos	15.0	2.0
0	40	neg	15.7	0.8
0	40	small	14.9	0.7
0	40	pos	14.3	0.5
0	30	neg	15.8	2.0
0	30	small	15.6	1.5
0	30	pos	15.0	0.0

TABLE C.2: **Binned radius data for high and low spin regimes at different inclinations.**

Spin Regime (a)	Inclination (i)	GR Deviation (ϵ)	Mean (px)	Std Dev (px)
low	90	0.4	15.5	0.7
high	90	0.4	14	undef
low	80	0.4	15.7	0.6
high	80	0.4	15	0
low	70	0.4	14.7	0.6
high	70	0.4	14.6	0.5
low	60	0.4	14.6	0.5
high	60	0.4	14.5	0.6
low	50	0.4	14	0
high	50	0.4	14.5	1
low	40	0.4	14.5	0.7
high	40	0.4	14	undef
low	30	0.4	14.6	undef
high	30	0.4	14.3	0.5

Bibliography

[1] K. Beckwith and C. Done. Extreme gravitational lensing near rotating black holes. *MNRAS*, 359:1217, 1228, 2005.

[2] G. C. Bower, H. Falcke, R. M. Herrnstein, J. Zhao, W. M. Goss, and D. C. Backer. Detection of the Intrinsic Size of Sagittarius A* Through Closure Amplitude Imaging. *Science*, 304:704–708, April 2004.

[3] H. Bradt. *Astronomy Methods: A Physical Approach to Astronomical Observations.* Cambridge University Press, 2004.

[4] A. E. Broderick, V. L. Fish, S. S. Doeleman, and A. Loeb. Evidence for Low Black Hole Spin and Physically Motivated Accretion Models from Millimeter-VLBI Observations of Sagittarius A*. *ApJ*, 735:110–115, 2011.

[5] A. E. Broderick, A. Loeb, and R. Narayan. The Event Horizon of Sagittarius A*. *ApJ*, 701:1357–1366.

[6] B. F. Burk and F. Graham-Smith. *An Introduction to Radio Astronomy, Second Ed.* Cambridge University Press, 2002.

[7] B. Carter. Axisymmetric Black Hole Has Only Two Degrees of Freedom. *Phys. Rev. Lett.*, 25(6):331–333, 1971.

[8] S. Doeleman, editor. *The EHT - status, goals, developments.* Bringing Black Holes into Focus: The Event Horizon Telescope, 2012.

[9] S. Doeleman et. al. Event-horizon scale structure in the supermassive black hole candidate at the Galactic Center. *Nature*, pages 78–80, 2008.

[10] S. Doeleman et. al. Detecting Flaring Structures in Sagittarius A* with High-Frequency VLBI. *ApJ*, pages 59–74, 2009.

[11] H. Falcke, F. Melia, and E. Agol. Viewing the Shadow of the Black Hole at the Galactic Center. *ApJL*, 528:13–16, 2000.

[12] V. Fish et. al. 1.3 mm Wavelength VLBI of Sagittarius A*: Detection of Time-Variable Emission on Event Horizon Scales. *ApJL*, pages 727–733, 2011.

[13] R. Geroch. Multipole Moments. II. Curved Space. *J. Math. Phys.*, 11:2580, 1970.

[14] S. Gillessen, F. Eisenhauer, T. K. Fritz, H. Bartko, K. Dodds-Eden, O. Pfuhl, T. Ott, and R. Genzel. The Orbit of Star S2 around Sgr A* from Very Large Telescope and Keck Data. *ApJL*, 707:L114–L117, 2009.

[15] R. O. Hansen. Multipole moments of stationary space times. *J. Math. Phys.*, 15:46, 1974.

[16] J. Illingworth and J. Kittler. A survey of the hough transform. *Computer Vision, Graphics, and Image Processing*, 44:87–116, 1988.

[17] M. J. Ireland, J. D. Monnier, and N. Thureau. Monte-Carlo Imaging for Optical Interferometry. In *Advances in Stellar Interferometry*, volume 6268 of *Proceedings of the SPIE*, page 62681T, 2006.

[18] T. Johannsen and D. Psaltis. Testing the No-Hair Theorem with Observations in the Electromagnetic Spectrum. II. Black Hole Images. *ApJ*, 718:446–454, 2010.

[19] P. Kierkegaard. A method for detection of circular arcs based on the Hough transform. *Machine Vision and Applications*, 5:249–263, 1992.

[20] J. McClintock and R. Remillard. *Black Hole Binaries*, chapter 4. 2004.

[21] A. V. Oppenheim and J. S. Lim. The importance of phase in signals. *Proc. IEEE*, 69:529–541, May 1981.

[22] S. C. Pei and J. H. Horng. Circular arc detection based on the Hough transform. *Pattern Recognition Letters*, 16:615–625, 1995.

[23] C. Reynolds and M. Nowak. Fluorescent iron lines as a probe of astrophysical black hole systems. *Physics Reports*, 377:389–466, 2003.

[24] D. C. Robinson. Uniqueness of the Kerr Black Hole. *Phys. Rev. Lett.*, 34(14):905–906, 1975.

[25] P. Schneider, J. Ehlers, and E. E. Falco. *Gravitational Lenses*. Springer-Verlag, 1999.

[26] A. R. Thompson, J. M. Moran, and G. W. Swenson, Jr. *Interferometry and Synthesis in Radio Astronomy*. John Wiley & Sons, Inc., 2001.

[27] K. S. Thorne. Multiple expansions of gravitational radiation. *Rev. Mod. Phys.*, 52:299, 1980.

[28] C. M. Will. *Was Einstein Right?* Basic Books, Inc., Publishers, 1986.

[29] C. M. Will. The confrontation between general relativity and experiment. *Living Reviews in Relativity*, 9(3), 2006.

[30] D. Young. Hough transform for circles, 2010.

[31] F. Zernike. The concept of degree of coherence and its application to optical problems. *Physica*, 5:785–795, August 1938.